

Banner appropriate to article type will appear here in typeset article

On the concentration distribution in turbulent thermals

Ludovic Huguet^{1,2} Victor Lherm³, Renaud Deguen¹, Joris Heyman⁴ and Tanguy Le Borgne⁴

¹ISTerre, Université Grenoble Alpes, Université Savoie Mont Blanc, CNRS, IRD, Université Gustave Eiffel, 38000 Grenoble, France

²Now at School of Earth and Environment, University of Leeds, Leeds LS2 9JT, UK

³Université Paris-Saclay, CNRS, FAST, 91405, Orsay, France

⁴Univ. Rennes, CNRS, Géosciences Rennes (UMR6118), 35042 Rennes, France

(Received xx; revised xx; accepted xx)

Turbulent thermals emerge in a wide variety of geophysical and industrial flows, such as atmospheric cumulus convection and pollutant dispersal in oceans and lakes. They form when a volume of buoyant fluid, arising from thermal or compositional density differences, is instantly released from a source. As they rise or sink, heat and mass transfers are likely to occur with the surrounding environment, spanning multiple scales from macroscopic entrainment of ambient fluid to microscopic diffusive processes. Although turbulent thermals are typically investigated through their integral properties, mixing processes specifically depend on the internal distribution of concentration or temperature. Here, we use laboratory fluid dynamics experiments and direct numerical simulations to investigate the mixing of a passive scalar in turbulent thermals with large Reynolds numbers. We track the evolution of the concentration field, computing its moments and the probability density function. The concentration distribution exhibits self-similarity over time, except at high concentrations, possibly because of the presence of undiluted cores. These distributions are well approximated by an exponential probability density function. In the investigated range, we find that concentration distributions are largely independent of the Péclet and Reynolds numbers.

Key words:

1. Introduction

A finite volume of buoyant fluid evolving under the influence of gravity in an otherwise quiescent environment forms what is called a *turbulent thermal* when the flow is turbulent. The term *thermal* originates from the terminology used by glider pilots, referring to a volume of warm air rising through the atmosphere (Scorer 1957; Woodward 1958). Turbulent thermals are fundamental elements of atmospheric convection and have been extensively studied by both the fluid dynamics and atmospheric science communities (Batchelor 1954; Blyth et al. 2005; Yano 2014). Yet the interest in turbulent thermals also extends to other contexts. Flows sharing strong similarities with atmospheric thermals can also develop in liquid environments, without being necessarily driven by temperature-induced density variations. The nature of the buoyancy forces — whether due to temperature variations, compositional differences, or the presence of multiple phases with differing densities — appears to be of secondary importance for the overall behavior of the thermal (Batchelor 1954; Turner 1979; Bush et al. 2003; Landeau et al. 2014).

Field observations and laboratory experiments show that turbulent thermals expand and decelerate as they rise, as a result of the gradual entrainment of ambient fluid (Batchelor 1954; Scorer 1957; Woodward 1959). This is consistent with dimensional analysis (Batchelor 1954), which predicts that far from the source the thermal radius r , velocity w , and reduced gravitational acceleration (or local buoyancy) g' evolve with distance z and time t as

$$r \sim z \sim \mathcal{B}_0^{1/4} t^{1/2}, \quad (1.1)$$

$$w \sim \mathcal{B}_0^{1/2} z^{-1} \sim \mathcal{B}_0^{1/4} t^{-1/2}, \quad (1.2)$$

$$g' = \frac{\Delta\rho}{\rho_a} g \sim \mathcal{B}_0 z^{-3} \sim \mathcal{B}_0^{1/4} t^{-3/2}. \quad (1.3)$$

where ρ_a is the density of the ambient fluid, $\Delta\rho$ the difference between the average density of the thermal and the ambient at time t , and g is the acceleration of gravity. \mathcal{B}_0 is the total buoyancy of the thermal, defined as

$$\mathcal{B}_0 = \frac{\Delta\rho_0}{\rho_a} g V_0, \quad (\text{m}^{-4} \text{s}^{-2}) \quad (1.4)$$

where $\Delta\rho_0$ is the value of $\Delta\rho$ at release, and V_0 the initial volume of the thermal. Equation 1.1 predicts that the size of the thermal increases in proportion to the distance traveled by the thermal, while equations 1.2 and 1.3 predict that the velocity and buoyancy decrease with distance and time, which results from the gradual dilution of the momentum and buoyancy of the thermal implied by entrainment of ambient fluid.

It is instructive to analyze the implications of equations 1.1-1.3 for the evolution with z of the different terms of the momentum conservation equation. Assuming that velocity fluctuations vary over a length scale $\sim r$, a scale analysis of the different terms of the momentum conservation equation shows that inertia scales as $\mathbf{v} \cdot \nabla \mathbf{v} \sim \mathcal{B}_0 z^{-3}$, buoyancy $g' \sim \mathcal{B}_0 z^{-3}$, and viscous forces $\nu \nabla^2 \mathbf{v} \sim \nu \mathcal{B}_0^{1/2} z^{-3}$ (ν denotes kinematic viscosity). The ratio of inertia to viscous forces, which defines an instantaneous Reynolds number Re , is constant in time (Scorer 1957; Johari 1992; Morton et al. 1994) and given by

$$\frac{\text{inertia}}{\text{viscous force}} \sim Re = \frac{\mathcal{B}_0^{1/2}}{\nu}. \quad (1.5)$$

If the buoyancy originates from a concentration field c with diffusivity D , one can easily infer, that the scaling laws 1.1-1.3 (with $g' \propto c$) imply that the advection and diffusion terms $\mathbf{v} \cdot \nabla c$ and $D \nabla^2 c$ of the transport equation for c are both $\propto z^{-5}$ when estimated for concentration

variations over a length scale $\sim r$. Their ratio, which defines an instantaneous Péclet number Pe , is constant and given by

$$\frac{\text{inertia}}{\text{diffusion}} \sim Pe = \frac{\mathcal{B}_0^{1/2}}{D}. \quad (1.6)$$

The same conclusion is reached if buoyancy originates from temperature rather than compositional variations. Note that the scaling given in equations 1.5 and 1.6 for the Reynolds and Péclet numbers can also be obtained from their usual definitions, $Re = wr/\nu$ and $Pe = wr/D$, using the scaling laws 1.1 and 1.2 for r and w .

The fact that the instantaneous Reynolds and Péclet numbers are constant suggests that turbulent thermals can evolve in a self-similar way when far from the source, in the sense that velocity and concentration or temperature would each have similar distributions at different times or distances from the source. This is consistent with early experimental determinations of the mean velocity field (Woodward 1959), and with experimental observations showing that the shape of thermals is often self-preserved (Scorer 1957).

However, some experimental observations argue against true self-similarity. Bond & Johari (2010) found that the vorticity within turbulent thermals tends to be localized in thin vortex cores, the width of which increases more slowly than the thermal radius. This was confirmed by Zhao *et al.* (2013), who also found that the maximum concentration within the thermal decreases at a much slower rate than predicted for the average concentration according to 1.3. Note also that the scaling laws 1.1-1.3, which imply constant Re and Pe , assume that the total buoyancy of the thermal is conserved. Experiments and numerical simulations show that detrainment (*i.e.* loss of mass and buoyancy) is small (Johari 1992; Lecoanet & Jeevanjee 2019; Morrison 2025) but not inexistent (an order of magnitude smaller than entrainment according to Lecoanet & Jeevanjee (2019)). This implies that the instantaneous Re and Pe decrease with time, albeit slightly, which does not allow perfect self-similarity.

The question of self-similarity is also related to the dynamics of mixing and homogenization of thermal or compositional heterogeneities, which sets the distribution of temperature or concentration within the thermal. The process of mixing involves the irreversible transformation of initially segregated phases into a homogeneous state (*e.g.* Villiermaux 2019). Unlike confined mixtures, a state of complete homogeneity can never be achieved in an expanding turbulent thermal due to the continuous entrainment of the surrounding fluid. The competition between homogenization, driven by stirring motions, and the production of compositional heterogeneities through the entrainment of surrounding fluid determines the degree of mixing within a thermal. A self-similar evolution would require that these two processes are in balance.

To our knowledge, the statistical distribution of the concentration or temperature field in a turbulent thermal has not yet been investigated, at least not in any systematic way. Numerical simulations of well-developed turbulent thermals (Lai *et al.* 2015; Lecoanet & Jeevanjee 2019; McKim *et al.* 2020; Orlandi & Carnevale 2020; Vybhav & Ravichandran 2022; Morrison *et al.* 2022; Middleton & Mumford 2023; Morrison *et al.* 2023; Morrison 2025) have predominantly investigated their global behavior in terms of the effects of moisture content on entrainment rates or the influence of stratification on thermal rise. Previous experimental work has also examined concentration measurements in puffs (Yee *et al.* 1994; Ghaem-Maghami & Johari 2006), plumes (Yee *et al.* 1995), and thermals (Bat *et al.* 1984; Marcus & Bell 1992; Zhao *et al.* 2013). However, they mostly provide global concentration measurements (Marcus & Bell 1992; Bond & Johari 2005, 2010; Zhao *et al.* 2013).

Our main goal here is to quantify the time-evolution of the distribution of the concentration or temperature field, as measured by their Probability Density Function (PDF), using laboratory experiments and numerical simulations at different Schmidt numbers $Sc = \nu/D$.

This provides a way of quantifying the approach to self-similarity as well as possible departures from self-similarity. It is also a first step towards a more detailed analysis of the dynamics of mixing within a turbulent thermal. The turbulent thermal, with its well-defined flow structure and its self-similar characteristics, is an interesting prototype for studying dispersion and mixing in an unconfined environment.

In this paper, we first revisit the dimensional analysis of turbulent thermals and propose predictions for the time evolution of the moments of the concentration field. In Section 3, we describe our experimental setup and numerical simulations, which were performed at Reynolds numbers up to $Re = 10^4$. Our direct 3D numerical simulations match the experimental Reynolds number but use a significantly lower Schmidt number ($Sc = 1$). We analyze the influence of Re and Sc on the evolution and distribution of the concentration field. Section 4 provides a qualitative description of turbulent thermals in experiments and simulations, including the definition of thermal boundaries and their dependence on concentration and vorticity thresholds. Section 5 presents a quantitative analysis of concentration distributions and moments, which suggests that the concentration field follows an exponential distribution far from the source. Finally, we discuss the effects of diffusivity (Sc) on concentration evolution in Section 5.4.

2. Dimensional analysis

2.1. Bulk properties

Consider a turbulent thermal formed by the release of a volume V_0 of a dense fluid, with density $\rho_a + \Delta\rho_0$, into an ambient fluid of density ρ_a . We denote by $d = (6V_0/\pi)^{1/3}$ the equivalent diameter at release (*i.e.* the diameter of a sphere of volume V_0). We assume that the density difference arises from fluctuations in concentration, but the following considerations also apply to thermally induced density variations, provided the Boussinesq approximation remains valid (*i.e.* small relative density variations, and negligible dissipative heating and compressibility effects). We denote by c_0 the initial concentration at release, in kilograms of solute per unit volume, and by $c(\mathbf{x}, t)$ the concentration at position \mathbf{x} and time t . D is the diffusivity of the concentration field, and ν is the kinematic viscosity, which we assume to be independent of concentration.

Previous experiments have shown that a turbulent thermal continuously entrains ambient fluid as it falls or rises (Batchelor 1954; Scorer 1957; Turner 1979; Zhao *et al.* 2013). As a result, the volume V of the thermal increases over time, while both its average concentration $\langle c \rangle$ and mean density difference $\Delta\rho$ relative to the surrounding fluid decrease (*e.g.* Batchelor 1954; Morton *et al.* 1956). Since the loss of material from the thermal is small (Lecoanet & Jeevanjee 2019), we assume that the mass of solute within the thermal, defined as $\mathcal{M} = \langle c \rangle V$, is conserved and equal to its initial value

$$\mathcal{M}_0 = c_0 V_0. \quad (2.1)$$

This implies that the total buoyancy $\mathcal{B} = \frac{\Delta\rho}{\rho_a} g V$ of the thermal is constant and equal to its initial value \mathcal{B}_0 as defined by equation 1.4.

In the Boussinesq approximation limit, a thermal is fully defined by V_0 , \mathcal{B}_0 , \mathcal{M}_0 , and by the transport properties ν and D . As shown by Batchelor (1954), dimensional analysis provides valuable predictions for the bulk properties of a thermal. For instance, the vertical position z_c of the center of mass of the thermal is a function of t , V_0 , \mathcal{B}_0 , \mathcal{M}_0 , ν , and D . This gives a set of seven quantities with three independent units. According to Vaschy-Buckingham's theorem, only four independent dimensionless quantities can be formed from these quantities, one

possible set being

$$\frac{z_c}{\mathcal{B}_0^{\frac{1}{4}} t^{\frac{1}{2}}}, \quad \frac{t}{t_g}, \quad Re = \frac{\mathcal{B}_0^{\frac{1}{2}}}{\nu}, \quad Pe = \frac{\mathcal{B}_0^{\frac{1}{2}}}{D}, \quad (2.2)$$

where t_g is a free-fall timescale defined as

$$t_g = \sqrt{\frac{\rho_a}{\Delta\rho_0} \frac{d}{g}} = \sqrt{\frac{\pi}{6} \frac{d^2}{\mathcal{B}_0^{\frac{1}{2}}}}. \quad (2.3)$$

This implies that $z_c \mathcal{B}_0^{-1/4} t^{-1/2}$ is a function of t/t_g , Re and Pe , or, equivalently, that

$$z_c = \mathcal{B}_0^{\frac{1}{4}} t^{\frac{1}{2}} f_z(t/t_g, Re, Pe), \quad (2.4)$$

where f_z is an unknown non-dimensional function. Similar analyses for the radius r of the thermal, its vertical velocity w , and its average concentration $\langle c \rangle$ yield

$$r = \mathcal{B}_0^{\frac{1}{4}} t^{\frac{1}{2}} f_r(t/t_g, Re, Pe), \quad (2.5)$$

$$w = \mathcal{B}_0^{\frac{1}{4}} t^{-\frac{1}{2}} f_w(t/t_g, Re, Pe), \quad (2.6)$$

$$\langle c \rangle = \mathcal{M}_0 \mathcal{B}_0^{-\frac{3}{4}} t^{-\frac{3}{2}} f_c(t/t_g, Re, Pe), \quad (2.7)$$

where f_r , f_w , and f_c are unknown non-dimensional functions. The prediction for $\langle c \rangle$ can also be derived from mass conservation $\langle c \rangle = c_0 V_0 / V \sim c_0 V_0 / r^3$, using (2.5) to express r .

In these equations, V_0 , \mathcal{B}_0 , \mathcal{M}_0 , and Re , Pe are conserved, time-independent quantities that do not depend on the release conditions of the dense fluid. In contrast, t_g is influenced by the specifics of the initial conditions. When far enough from the release point, the thermal is expected to become independent of its initial conditions (Batchelor 1954). In this limit, r , w , and $\langle c \rangle$ become independent of t_g . In addition, laboratory experiments and field observations of atmospheric thermals (*e.g.* Woodward 1958, 1959) and volcanic clouds (*e.g.* Terada & Ida 2007) have shown no measurable effect of Re and Pe on the time evolution of thermal size and velocity. When $t \gg t_g$, these assumptions imply that (Batchelor 1954; Morton *et al.* 1956)

$$z_c \sim \mathcal{B}_0^{\frac{1}{4}} t^{\frac{1}{2}}, \quad (2.8)$$

$$r \sim \mathcal{B}_0^{\frac{1}{4}} t^{\frac{1}{2}}, \quad (2.9)$$

$$w \sim \mathcal{B}_0^{\frac{1}{4}} t^{-\frac{1}{2}}, \quad (2.10)$$

$$\langle c \rangle \sim \mathcal{M}_0 \mathcal{B}_0^{-\frac{3}{4}} t^{-\frac{3}{2}}. \quad (2.11)$$

Combining equations (2.8) and (2.9) implies that the radius of the thermal is proportional to the distance it has traveled, which gives

$$r = \alpha z_c, \quad (2.12)$$

where α is the *entrainment coefficient* (Morton *et al.* 1956).

2.2. Moments of concentration

Using dimensional analysis along the same lines as in section 2.1, the moments of order k $\langle c^k \rangle$ of the concentration field can be expressed as

$$\langle c^k \rangle = \left(\mathcal{M}_0 \mathcal{B}_0^{-\frac{3}{4}} t^{-\frac{3}{2}} \right)^k f_{c,k}(t/t_g, Re, Pe), \quad (2.13)$$

where $f_{c,k}$ are unknown dimensionless functions.

As explained in section 2.1, we expect that the thermal becomes independent of its initial condition when far enough from the release point (Batchelor 1954). In this limit, when $t \gg t_g$, the moments become independent of t_g , which gives

$$\langle c^k \rangle = \left(\mathcal{M}_0 \mathcal{B}_0^{-\frac{3}{4}} t^{-\frac{3}{2}} \right)^k f_{c,k}(Re, Pe). \quad (2.14)$$

As a result, the moments of $c/\langle c \rangle$, expressed as

$$\langle (c/\langle c \rangle)^k \rangle = \frac{\langle c^k \rangle}{\langle c \rangle^k} = \frac{f_{c,k}(Re, Pe)}{f_{c,1}(Re, Pe)^k}, \quad (2.15)$$

are predicted to be independent of time, which implies that the probability density function (PDF) of $c/\langle c \rangle$ is also independent of time. Equivalently, this predicts that the PDF of c is expected to become self-similar in time when $t \gg t_g$. Since the moments of $c/\langle c \rangle$ depend on t/t_g close to the source (Eq. 2.13), this prediction does not hold in that region.

We can also express the moments of concentration as

$$\frac{\langle c^k \rangle}{c_0^k} = \left(\frac{t}{t_g} \right)^{-\frac{3}{2}k} f_{c,k}(Re, Pe). \quad (2.16)$$

This form has the inconvenience of artificially introducing parameters related to the source (c_0 and t_g) but will prove more convenient for comparison with experimental and numerical data (section 5).

The dimensional analysis on the moments of concentration (Eq. 2.14) implies that the shape of the PDF of c may vary with Re and Pe . As a result, we aim to evaluate the predictions for the time evolution of the moments of c and to investigate the effect of Re and Pe on the shape of its distribution. Although it has been convincingly argued that the bulk properties of the thermal are expected to be independent of viscosity and diffusivity (Taylor 1946; Batchelor 1954; Scorer 1957; Morton *et al.* 1956), this has yet to be tested for the concentration distribution.

3. Experiments and numerical simulations

3.1. Experiments

In our experiments, we release a volume of an aqueous solution of sodium chloride (NaCl) into a $30 \times 30 \times 100$ cm tank containing fresh water (figure 1). The NaCl solution is initially contained in aluminum tubes of varying diameter and height $s_0 = 15, 30, 45$, and 60 mm, corresponding to released volumes $V_0 = 2.7, 21.2, 71.6$, and 169.6 mL, respectively. We use the diameter d of the equivalent sphere of volume V_0 , *i.e.* $d = (3/2)^{1/3} s_0$, as a measure of the initial size of the released volume. We seal the tube at both ends with latex membranes stretched over the openings and proceed to fill it with the NaCl solution. We submerge the tube in the tank to a depth of approximately 15 cm below the surface, and we delicately pierce the upper membrane with a needle to release any trapped air bubbles. A negligible amount

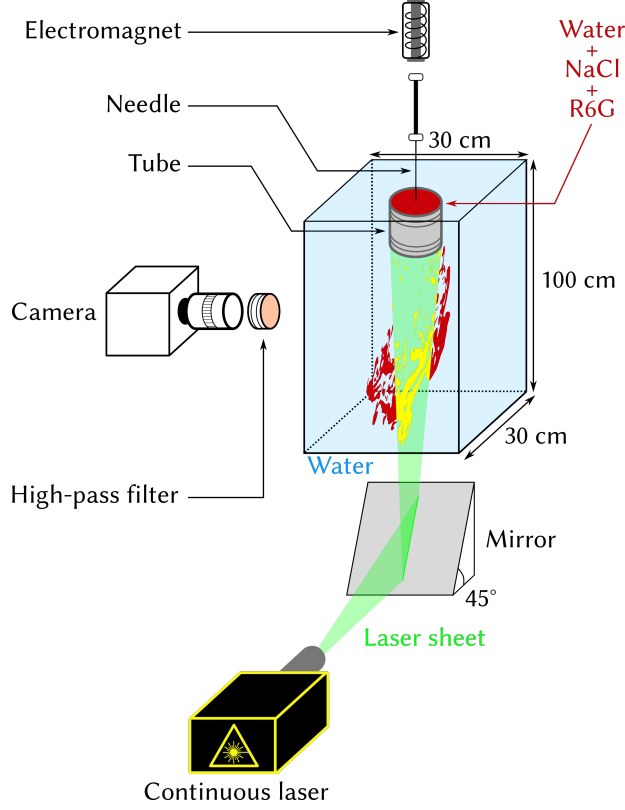


Figure 1: Schematic of the experimental setup using laser-induced fluorescence on a turbulent thermal flow.

of fluid is drawn out of the tube during the operation due to the retraction of the membrane. After a minute of rest, we release a needle previously held in place by an electromagnet and abruptly puncture the lower membrane, which retracts rapidly. The fluid contained in the tube is quickly released due to the density difference with the ambient fluid. For the 15 mm tube, we pierce both membranes simultaneously, as, in this case, the retraction of the upper membrane draws a non-negligible amount of fluid out of the tube. As a result, dense fluid is released from the top of the tube, significantly altering the initial conditions of the fluid release.

We obtain the concentration field of a fluorescent dye (Rhodamine 6G) initially mixed with the NaCl solution using Laser-Induced Fluorescence (LIF). We illuminate the tank from below with a vertical laser sheet (532 nm) produced by a continuous 400 mW Nd:YAG laser coupled with a cylindrical lens (figure 1). We image the LIF field using a PCO Edge 5.5 camera (2560×2160 pixels, 20 Hz, 16-bit dynamic range) fitted with a Nikon Nikkor 50 mm f/1.2 lens. We use a high-pass filter (> 540 nm) to remove the laser wavelength and isolate the emission signal of Rhodamine 6G (between 500 and 700 nm). We spatially calibrate the images using a grid, remove the background, and correct for laser sheet heterogeneities. Finally, we obtain the concentration field using a calibration between light intensity and concentration (Appendix A).

The field of view of the camera spans 32.8×38.5 cm (horizontal \times vertical). When scaled by the equivalent diameter d , this corresponds to fields of view of 19×22 , 10×11 , 6×7 , and 5×6 for tube diameters of 15, 30, 45, and 60 mm, respectively. The field of view starts

#	s_0 (mm)	d (mm)	$\Delta\rho_0/\rho_a$	\mathcal{B}_0 (m ⁴ /s ²)	μ_0/μ_a	Re	Pe
(A)	15	17.1	0.156	4.1×10^{-6}	1.62	2012	5.04×10^6
(B)	45	51.5	0.017	1.2×10^{-5}	1.05	3452	8.64×10^6
(C)	30	34.3	0.084	1.8×10^{-5}	1.25	4175	1.04×10^7
(D)	60	68.7	0.013	2.2×10^{-5}	1.04	4646	1.16×10^7

Table 1: Parameters used in the four types of experiments (A, B, C, and D) with $Sc = 2500$

at 5.3, 9.1, 8.3, and 7.6 cm below the bottom of the tube, which, when made dimensionless, gives 3.1, 2.6, 1.3, and 1.1 times the equivalent diameter.

Our experiments are divided into four categories, (A) to (D), depending on the tube used to release the dense fluid (Table 1). For each tube, we choose the NaCl concentration such that the Reynolds number is maximized while keeping a concentration low enough to prevent significant optical distortion when the thermal enters the field of view of the camera. We measure the density of the NaCl solutions using an Anton Paar 35 Basic densitometer, which has an accuracy of approximately 0.1%. We estimate viscosities and refractive indices from data compiled by Haynes (2014).

Table 1 gives the ratio $\Delta\rho_0/\rho_a$ selected for the four configurations corresponding to different tube diameters s_0 and equivalent sphere diameter d . The range of initial density differences corresponds to a range of total buoyancy \mathcal{B}_0 and translates into a viscosity range of $\mu_0 = 1.03 - 1.60$ mPa s and a refractive index range of 1.336 – 1.370. In comparison, the viscosity of fresh water is $\mu_a = 1.005$ mPa s and its refractive index is 1.333. However, it should be noted that the cloud formed by the NaCl solution is significantly diluted when it enters the field of view of the camera, resulting in variations of viscosity and refractive index that are significantly smaller than those suggested by the values mentioned above. The maximum viscosity corresponding to the maximum salt concentration of the thermal (see figure 5b), is up to 3% larger than the viscosity of water (1.6%, 2.3%, 3%, 3% for A, B, C, D cases). The average viscosity in the diluted thermal when it enters the field of view is then close to the water viscosity. Then, we neglect the effect of viscosity on the long-term evolution of the thermal and calculate the Re using the viscosity of the ambient fluid (see Eq. 2.2).

Péclet numbers are calculated from equation (2.2), using the diffusivity of Rhodamine 6G in water, estimated at $D^{rhod} = 4.0 \times 10^{-10}$ m² s⁻¹ (Gendron et al. 2008), for Pe . The diffusivity of sodium chloride, $D^{salt} = 1.5 \times 10^{-9}$ m² s⁻¹, is approximately 4 times larger than the diffusivity of Rhodamine 6G. As a result, we expect the salt concentration field to differ from the Rhodamine 6G concentration field measured with LIF. However, both diffusion coefficients give a large Schmidt number Sc (2500 and 6700, respectively).

In each configuration, we conducted and analyzed three experiments to estimate flow variability. The unsteady nature of the flow, as well as the coupling between buoyancy and mean flow, makes the early evolution of the thermal sensitive to the initial conditions resulting from puncturing the membrane that seals the tube. The lower membrane does not always retract in the same way, thereby affecting the initial conditions. In Section 5, we will show the evolution of concentration moments and PDF of concentration of the average of the three experiments for each Reynolds number.

3.2. Numerical simulations

We have conducted 3D simulations of thermals with the open-source pseudospectral code Dedalus (Burns et al. 2016, 2020), using the setup described by Lecoanet & Jeevanjee

(2019). The equations of conservation of momentum and concentration are solved under the Boussinesq approximation. The thermal is initialized at $t = 0$ by introducing a spherical concentration perturbation of diameter d into an otherwise homogeneous fluid. The spatial domain extends horizontally over $10d$ in both the x and y directions, and vertically over $20D$ in the z direction. It is respectively discretized in $256 \times 256 \times 512$ modes. We benchmark our simulations against a simulation with a higher resolution of $512 \times 512 \times 1024$, kindly provided by Daniel Lecoanet (Lecoanet & Jeevanjee 2019). At a given Reynolds number ($Re \approx 4631$), we find that the kinetic energy spectrum and PDF of concentration (figure 23) are very similar between the two resolutions.

Our numerical simulations use Reynolds numbers that match those of our experiments. In contrast, the Schmidt number Sc is set to 1 in all numerical simulations (for computational resource reasons), resulting in a concentration field that diffuses much faster than in the experiments, where $Sc = 2500$. Consequently, the Péclet number is also a factor 2500 larger in the experiments than in the simulations. It will allow us to investigate the effect of the Schmidt number on concentration distributions.

In each simulation, we extract two orthogonal planes that intersect in the middle of the grid. In Section 5, we will show the evolution of concentration moments and PDF for the average of these two orthogonal planes and compare them to the experiments performed at the same Reynolds numbers.

4. Qualitative description of a turbulent thermal

4.1. Macroscopic evolution

Figure 2 shows the evolution of the concentration field for a given $Re = 3452$ for one experiment and a simulation. The concentration scale changes between each time step for better visualization. During its fall, the radius of the turbulent thermal increases as the surrounding liquid is entrained and incorporated into the thermal (figure 2a,b), a phenomenon referred to as turbulent entrainment. We observe the interaction between a large-scale engulfment, producing an entraining flow behind the thermal, and the development of small-scale turbulent fluctuations. As a result, turbulent entrainment progressively dilutes the fluid within the thermal, through stirring and mixing processes. In both experiments and simulations, we find that the radius of the thermal increases with depth in an approximately linear way, in agreement with the prediction of equation 2.12 (Appendix figure 12). All experiments (except the one at the lowest Reynolds) and simulations have close to an entrainment coefficient α of 0.18, which is in agreement with previous experimental and numerical studies with an aspect ratio of the source equal to 1 (Lecoanet & Jeevanjee 2019; Bond & Johari 2010; Lai et al. 2015). While both experiments and simulations evolve similarly at large scale, in the close-up snapshots (figure 2c,d), we observe significant differences in the scale of the structures inside the turbulent thermal which are probably due to the difference of Schmidt number (see discussion in Sec. 5.4).

4.2. Anatomy of a turbulent thermal

In this section, we describe the anatomy of a turbulent thermal and investigate the concentration distribution in its different parts. We consider concentration fields from an experiment and a simulation at the same Reynolds number ($Re = 4175$), and we focus on snapshots far from the source, *i.e.* $t/t_g = 51.25$ in the experiment and $t/t_g = 31.6$ in the simulation. In the following, the concentration is normalized by the initial concentration c_0 .

A buoyant thermal is composed of a head, containing most of the initial buoyant fluid, followed by a turbulent wake. The head has an ellipsoidal shape flattened in the vertical

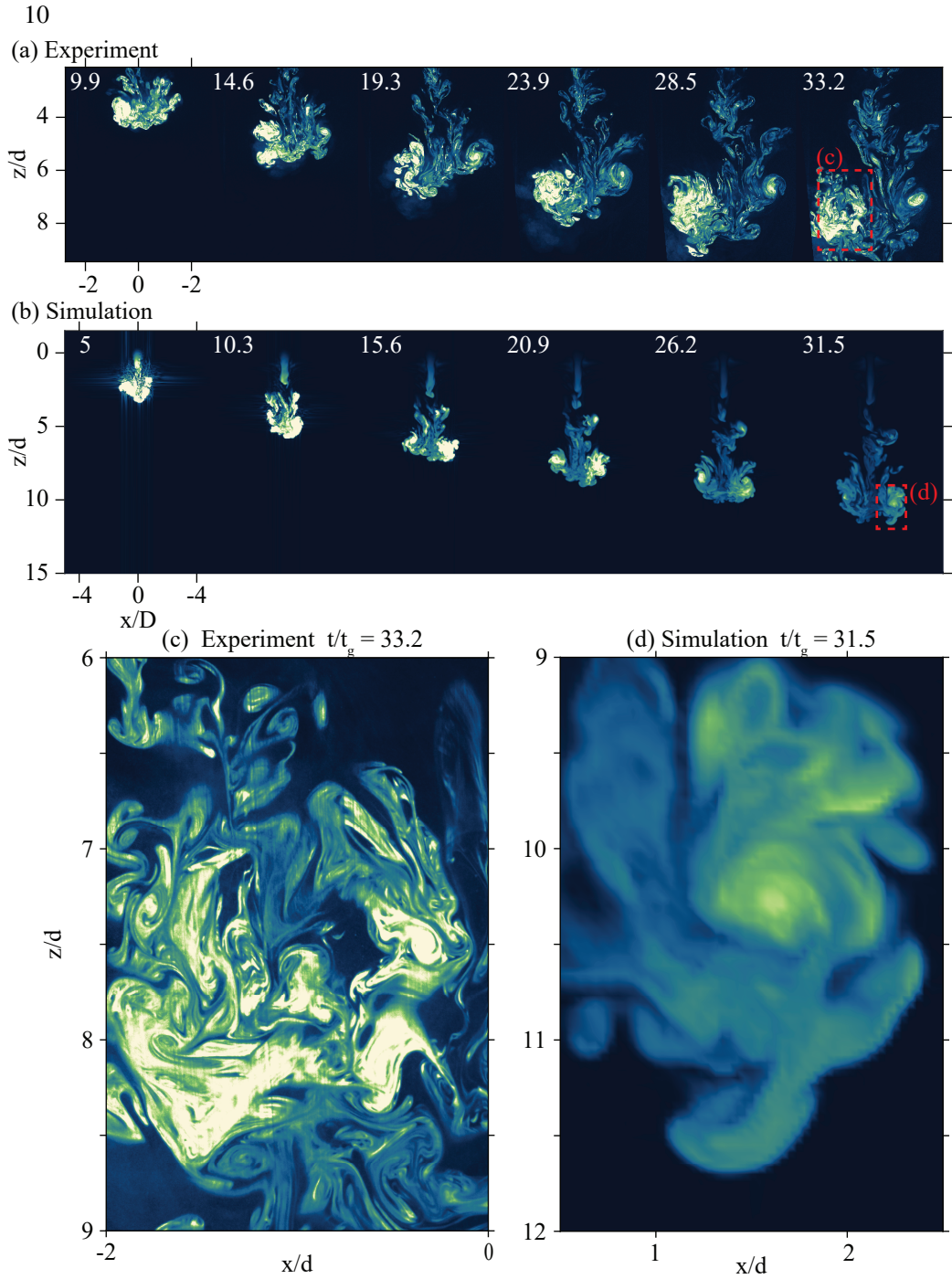


Figure 2: (a,b) Evolution of a turbulent thermal for experiments with Reynolds number Re equal to 3452 for an experiment and a simulation, respectively. On each image, the time is normalized by t_g . (c,d) Close-up snapshots of the last time-step for the experiment (a) and simulation (b).

direction. It consists of a vortex ring, the so-called cores of the thermal, and a peripheral region where the surrounding fluid is entrained in the thermal. The regions with high values of concentration are the undiluted cores (Blyth *et al.* 1988; Romps & Kuang 2010).

Although turbulent thermal structures are qualitatively well-defined, tracking their position, shape, and contour may be quantitatively challenging. In a miscible thermal, the entrainment of the surrounding fluid and the diffusion of buoyant fluid complicate the definition of its contour. Previous works implemented various methods, from an ellipsoidal shape defined by the horizontal and vertical average of the buoyancy field (Zhao *et al.* 2013; Lecoanet & Jeevanjee 2019), to more sophisticated methods (Romps & Charn 2015; McKim *et al.* 2020). Overall, the envelope of the thermal depends on a threshold value of the buoyancy field (temperature, concentration, or density).

Figures 3 and 4 show the effect of the definition of the boundary of the thermal on its spatial extent and the concentration distribution. We investigate two different ways of defining the limits of the thermal: a tight threshold corresponding to a concentration equal to a fixed fraction 0.5 of $\langle c \rangle$, the average of c within the thermal defined by the mask, and a loose definition of the thermal limit corresponding to the same threshold with a dilation operation using the morphological structuring element. The threshold value is the same for all experiments and simulations; it is constant in terms of the value of $c/\langle c \rangle$, but time-dependent in terms of c . The reasons for this choice are explained in section 5.2. Both masks include concentration values of the head, cores, and wakes of the thermal.

Figure 3a shows a turbulent thermal at $t/t_g = 51.25$ and for $Re = 4175$ and the two masks. The mask for a tight threshold is split into two parts (by a given z/D): the head of thermal and the wake. The experimental values of concentration are limited by the dynamic range of the camera (16-bit resolution), and they contain a maximum of 5 orders of magnitude in intensity variation. In figures 3b,c, we compare the histograms of the concentration values and the probability density functions of the different regions in the thermal. Most of the concentration values are below 10^{-3} and correspond to the background values outside the thermal (figure 3b). The histograms of the whole field view and both masks are very similar for concentration values above 10^{-3} . The two parts (head and wake) of the tight mask show the same shape in the PDF (figure 3b), except there are no extreme values of concentration in the wake. These extreme values come for the most part from the cores inside the head, as already observed in previous experiments (Johari 1992). Figure 3 shows that the loose mask includes values that are part of the background or surrounding fluid. Therefore, the shape of the PDF below 10^{-3} depends significantly on the image analysis, especially on the pixel size used in the morphological structuring element.

In figure 4, we have applied the same threshold and mask to a simulation (with the same Reynolds number, at $t/t_g = 31.6$). We reduced the size of the morphological structuring element to take into account the lower resolution of the simulation (figure 4a). While experiments have a camera-limited range of concentration values, the histogram of concentration values extends over 8 orders of magnitude in the simulation. For a concentration value above 10^{-2} , the histograms of loose and tight masks are very similar. Most of the high values of concentration correspond to the cores of the thermal inside the head (figure 4b). In figure 4b, the PDF of the smallest values (between 10^{-8} and 10^{-5}) decreases as $1/c$, which is a characteristic of the initial noise at $t/t_g = 0$. The values of concentration between 10^{-5} and 10^{-2} are surrounding the thermal defined by the tight mask. The shape of the PDF for these values depends significantly on the image processing used to define the mask.

Based on figure 3 and 4, we have chosen to analyze our data using the tight threshold. Figure 3c and 4c show semi-log versions of the PDF of concentration, which highlights its shape for the values above 10^{-3} . It suggests that the PDF of c decreases exponentially at

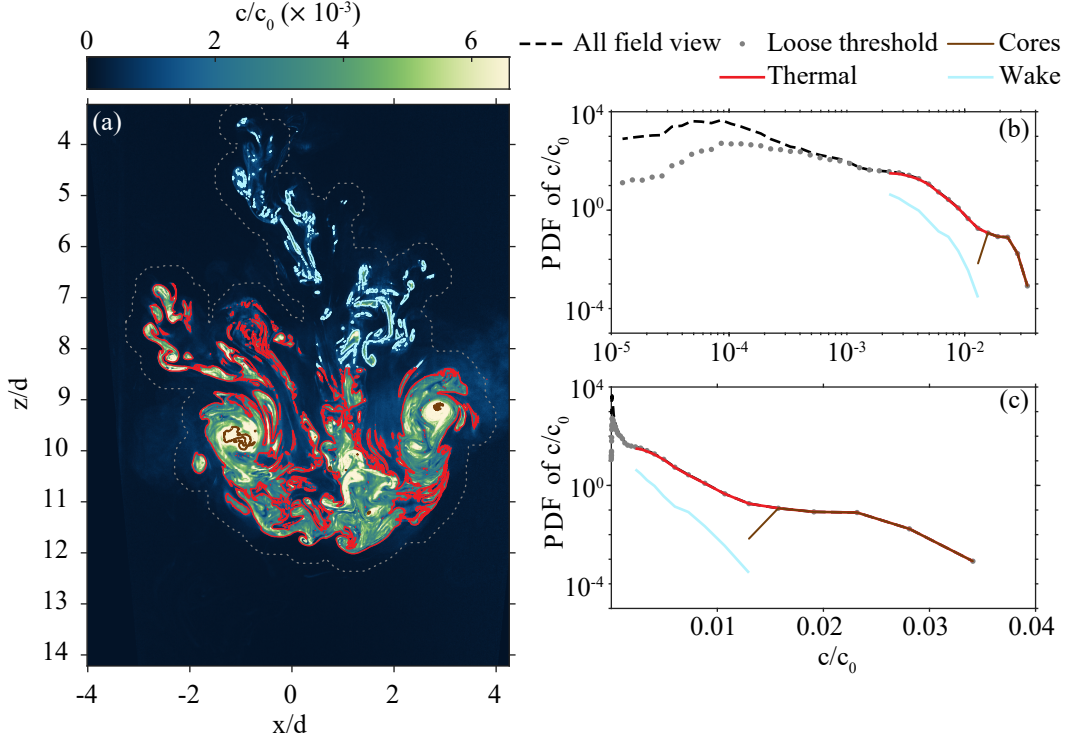


Figure 3: (a) Snapshot of the concentration field at $t/t_g = 51.25$ for one of the three experiments at $Re = 4175$. Colored lines denote the mask applied on the snapshot to produce the PDF of the concentration in (b, c). (b) and (c) PDF of the concentration as a function of the concentration in log-log or semi-log, respectively. The dashed black line represents the PDF of the whole snapshot. The gray dotted line shows the PDF of the thermal using a loose threshold. The inside of the thermal comprises all pixels inside the cyan and red masks. Brown and cyan lines in (b,c) (and mask in (a)) denote the different parts of the thermal: wake and cores, respectively.

intermediate values of c , between the threshold and an upper value which is ≈ 0.013 and ≈ 0.03 in the experiment (figure 3b) and simulation (figure 4b) snapshots. The figures suggest that the deviations from the exponential PDF at high concentrations can be attributed to the cores. In contrast, the distribution in the wake seems to be well described by an exponential PDF.

5. Evolution of PDF and moments of concentration

In this section, we investigate the moments and PDF of the concentration. We will examine the time dependence from the release of the buoyant fluid (for the simulations) to large distances and times after the release ($t/t_g > 10$). We will also compare the differences and similarities between experiments and simulations that have been performed at the same Reynolds numbers but very different Péclet numbers. In what follows, the concentration is normalized by the initial concentration $c_0 = c(t = 0)$.

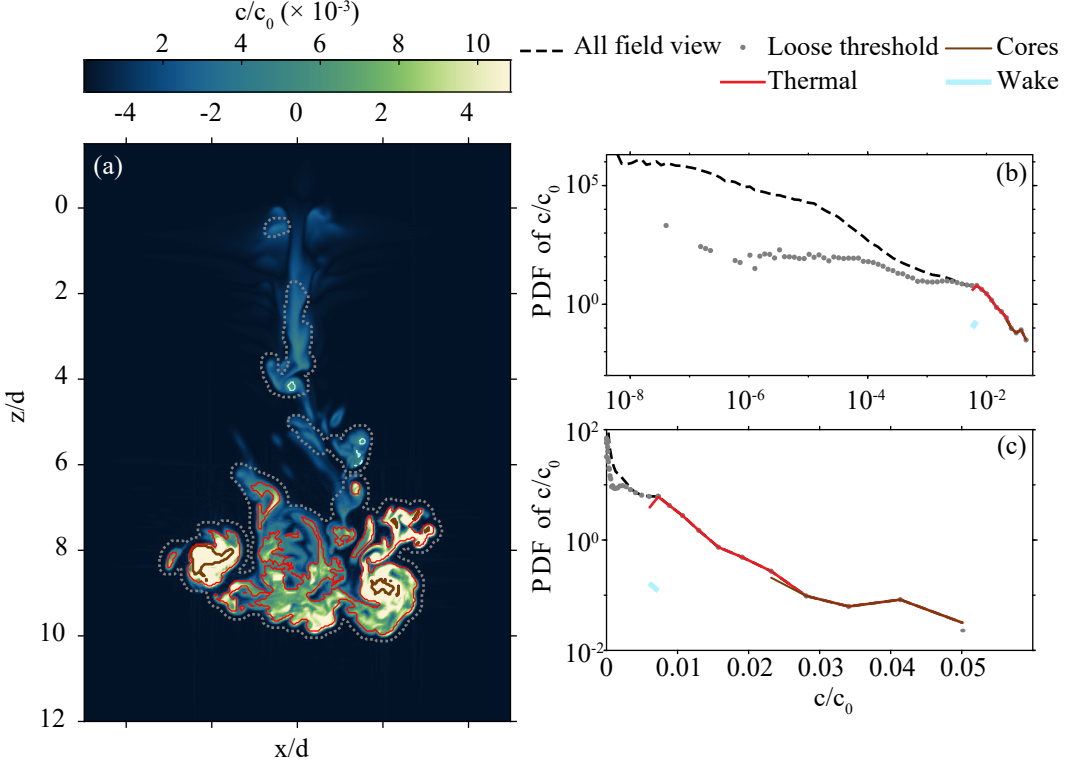


Figure 4: (a) Snapshot of the concentration field at $t/t_g = 31.6$ for one of the simulations at $Re = 4175$. Colored lines denote the mask applied on the snapshot to produce the PDF of the concentration in (b, c). (b) and (c) PDF of the concentration as a function of the concentration in log-log or semi-log, respectively. The dashed black line represents the PDF of the whole snapshot. The gray dotted line shows the PDF of the thermal using a loose threshold. The inside of the thermal comprises all pixels inside the cyan and red masks. Brown and cyan lines in (b,c) (and mask in (a)) denote the different parts of the thermal: wake and cores, respectively.

5.1. Moments of concentration

Figure 5a,b shows the mean concentration $\langle c/c_0 \rangle$, the maximum concentration against time, for all experiments and simulations. These are calculated from $t = 0$ in the simulations, but we only focus on $t/t_g > 1$. At larger t/t_g , the mean decreases following a power law close to $t^{-3/2}$, in agreement with the prediction of dimensional analysis (Eq. (2.16)). Since the concentration is averaged within each pixel, the absolute value of the maximum depends on the resolution of the concentration structures inside the thermal. In addition, the number of pixels covering the thermal is not constant, as the thermal radius increases as the square root of time. For example, in the simulations, there are five times more pixels per thermal radius at $t/t_g = 30$ than at $t/t_g = 0$. We quantified this effect by progressively reducing the resolution of a simulation over time, *i.e.*, maintaining a constant number of pixels per thermal radius. From this, we conclude that the evolution of the maximum concentration observed in figure 5b is meaningful, *i.e.* the decrease of maximum concentration is not a geometrical artifact. For both experiments and simulations, the maximum concentration decreases more slowly than the mean concentration. The slopes of the maximum and mean concentrations seem similar between our experiments and simulations. However, the curves

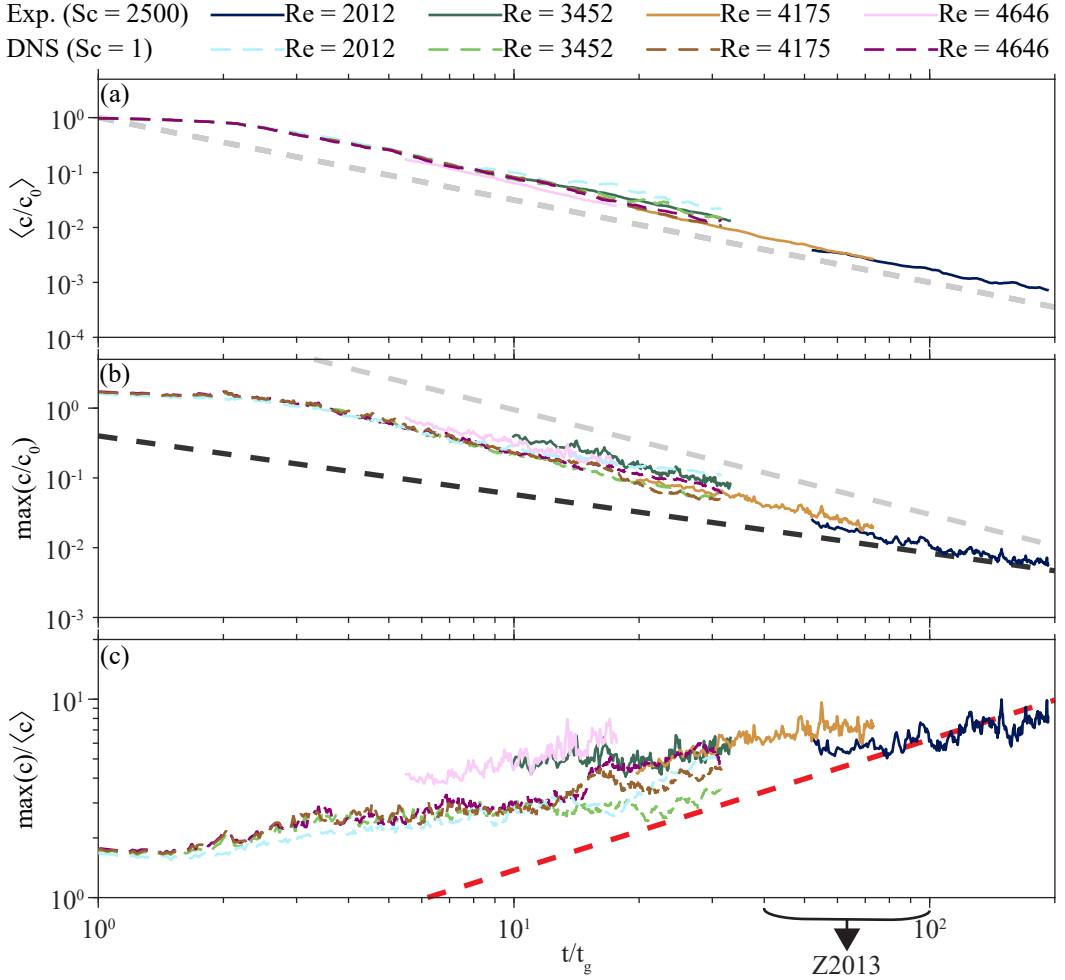


Figure 5: (a) Mean of concentration c/c_0 as a function of time t/t_g for the average of three experiments at each Re (solid lines) and the average of two simulations at each Re (dashed lines). (b) Maximum concentration c/c_0 as a function of time t/t_g . In (a) and (b), the gray and black dashed lines show the power laws $t^{-3/2}$ and $t^{-0.84}$ as in Zhao et al. (2013). (c) The ratio between the maximum concentration and its mean as a function of time t/t_g . The red dashed line shows the ratio of the two previous power laws. Results of Zhao et al. (2013) (Z2013) span only between 40 and 100 t/t_g . Note that all power laws intend to show the slope, i.e., they have an arbitrary pre-factor.

seem to be offset in time from one another. This might be due to the variation in the initial condition, which determines the value of t_g and the time origin. We also found that these slopes agree reasonably well with the power-law fit from previous experiments for a similar Reynolds number (Zhao et al. 2013). Note that the fit from (Zhao et al. 2013) is obtained in a short time range. Figure 5c shows that the ratio between the maximum and the instantaneous concentration mean increases with time, which is consistent with the thermal cores evolving separately from the bulk of the thermals. The maximum concentration compared to the concentration's mean in the simulations is smaller than in the experiments, which can be interpreted as the effect of a higher diffusion rate in the simulation.

Figure 6 shows the k th moments of the concentration ($k = 1, 2, 4, 6, 8$) over time. For

Exp. (Sc = 2500) Re = 2012 Re = 3452 Re = 4175 Re = 4646
 DNS (Sc = 1) Re = 2012 Re = 3452 Re = 4175 Re = 4646

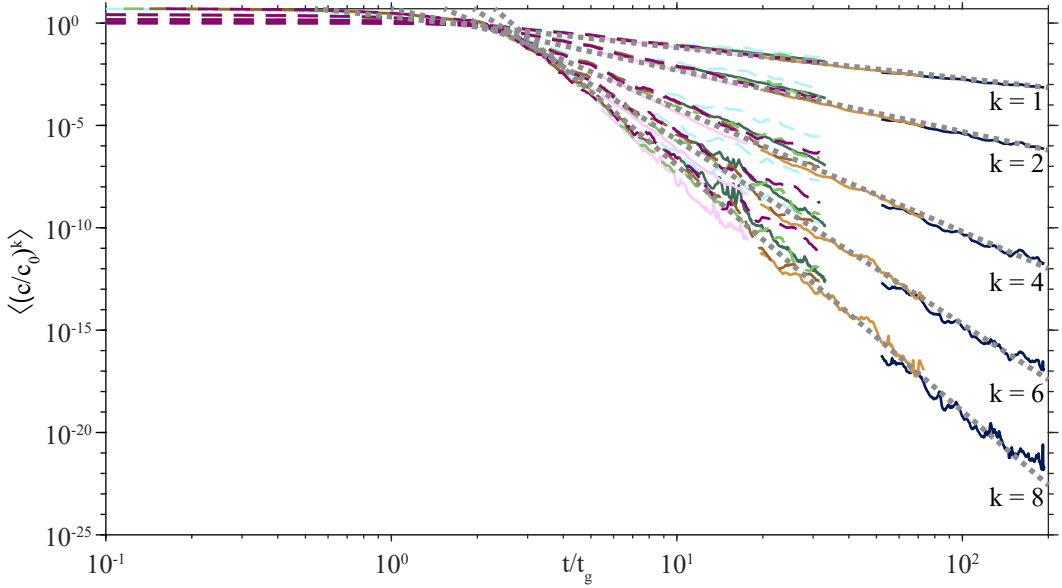


Figure 6: Moment of concentration c^k , with $k = 1, 2, 4, 6, 8$ as a function of time t/t_g for the average of three experiments at each Re (solid lines) and the average of two simulations at each Re (dashed lines). The gray dotted lines show the moments as predicted by dimensional analysis and the exponential shape of the PDF (Eq. 5.7).

each Reynolds number, we average three experiments and two simulations. The dashed grey lines show the predictions of the dimensional analysis (Eq. 2.16) for the time evolution of the moments, $\langle c^k \rangle \sim \left(\frac{c_1 t}{t_g} \right)^{-\frac{3}{2}k}$. The values of the prefactors ($c_1 = 20$) and the implications for the shape of the PDF will be discussed in subsection 5.2. The time evolution of the moments is in good agreement with the predictions from dimensional analysis. Although the 8th moment of concentration decreases by 20 orders of magnitude over the investigated time interval, Eq. 2.16 still accurately predicts its evolution.

5.2. PDFs of concentration

We have calculated the probability density function of the concentration as a function of time for all the experiments and simulations. The 100 bins of the PDF are logarithmically spaced between the minimal concentration values and 1 for the concentration and between 5×10^{-1} and $\times 10^5$ for the PDF of the concentration normalized by the mean concentration $\langle c \rangle$. Figure 7 represents these PDFs for a given experiment and a simulation, with the same $Re = 3452$. The PDFs of c for all others Reynolds are shown in Appendix B (see figures 13, 14, 15). In figure 7, the first PDF that is plotted corresponds to $t/t_g \sim 10$ for the experiment, and $t/t_g = 0$ for the simulation, for which the concentration field is available from the start. In both cases, the PDFs of concentration exhibit a drift toward smaller concentration values, in agreement with the time evolution of $\langle c \rangle$ and $\max(c)$ (see figure 5a,b). For $t/t_g > 10$, the shape of the PDF seems to be relatively constant with time and qualitatively consistent between the simulations and the experiments.

Figure 6 confirms the prediction of the dimensional analysis that the moments evolve as

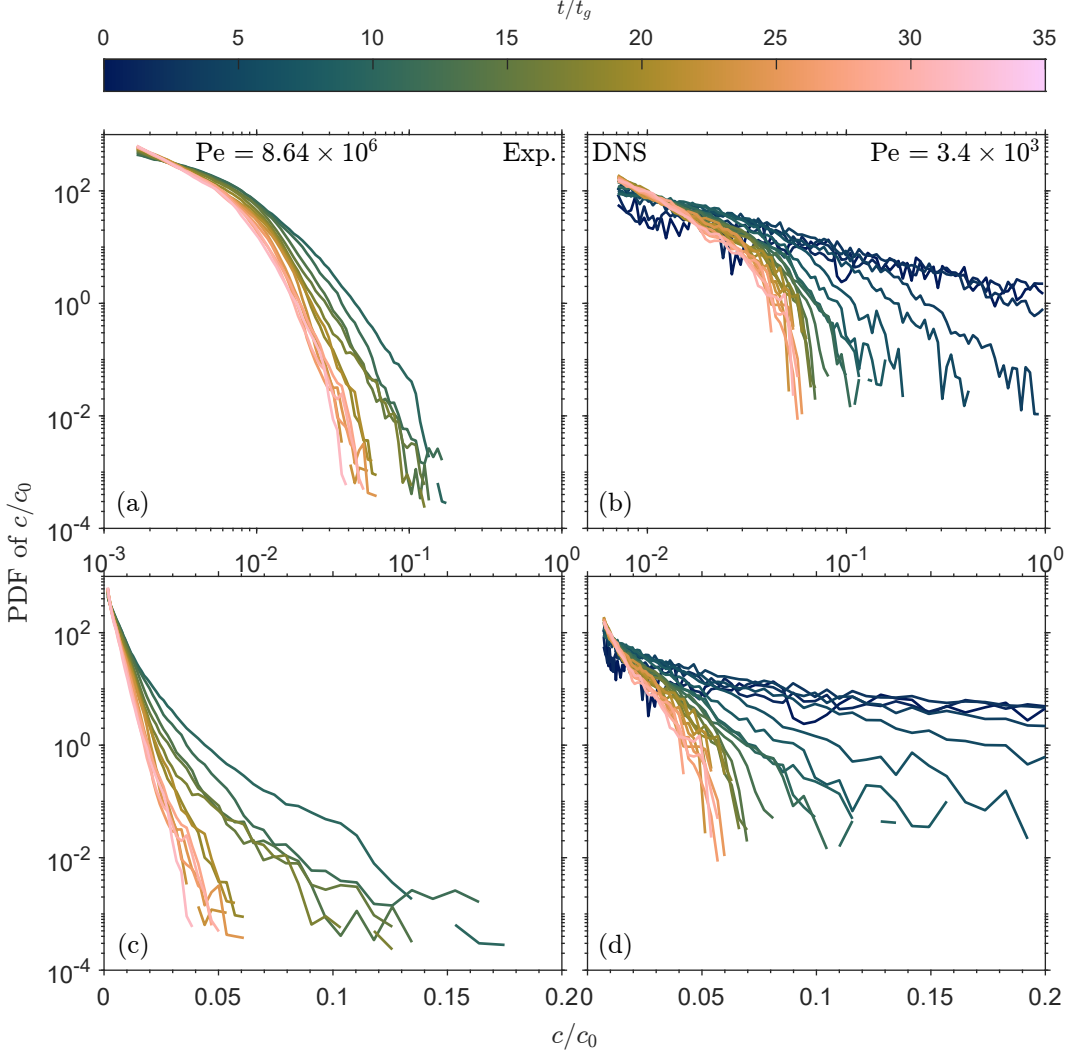


Figure 7: PDF of c as a function of c and time t/t_g for an experiment with $Re = 3452$ (a,c) ($Pe = 8.64 \times 10^6$) and a simulation with the same Re (b,d) ($Pe = 3.4 \times 10^3$). The top and bottom rows are log-log and semi-log plots, respectively.

$\sim t^{-\frac{3}{2}k}$. Following the discussion of section 2.2, one should therefore expect the PDF of $c/\langle c \rangle$ to be independent of time. Figure 8 shows the PDFs of $c/\langle c \rangle$ in a log-log space and semi-log space for an experiment and a simulation, with $Re = 3452$. Once normalized by $\langle c \rangle$, the PDFs of concentration for both simulation and experiment collapse (figure 8a,b), in agreement with the prediction of section 2.2.

A similar behavior is observed for all Reynolds number (see figures 16, 17, 18). In the simulations, the PDF initially exhibits a different shape for the first few t/t_g because the thermal is not yet fully developed. In addition, the concentration PDF remains nearly identical between simulations with the same Reynolds number but different resolutions (see in Appendix B figure 23).

5.3. Shape of the PDF of concentration

Figure 8 shows that the PDF is linear for intermediate values of $c/\langle c \rangle$ when plotted in semi-log, suggesting that the PDF has the shape of a decreasing exponential, at least in this concentration range. However, care must be taken when characterizing the underlying PDF. Assuming it is of the form $p(X = c/\langle c \rangle) = \beta \exp(-\lambda X)$ as suggested by our data, the parameters λ and β are fixed by the requirement that the integral of $p(c/\langle c \rangle)$ over the concentration domain is 1, and that the expectancy (i.e. first moment) of $c/\langle c \rangle$ is 1. If $c \in [0, \infty]$, then $\lambda = \beta = 1$ and, if exponential, the PDF of $c/\langle c \rangle$ is

$$p(X = c/\langle c \rangle) = \exp(-X). \quad (5.1)$$

However, the PDFs we have calculated are lower-bounded by the threshold value used to define the thermal, which is given by a fixed value ξ of the ratio between the concentration and the mean. Imposing that $\int_{\xi}^{\infty} p(X = c/\langle c \rangle) dX = 1$ and $\int_{\xi}^{\infty} p(X = c/\langle c \rangle) X dX = 1$, we find that, if exponential, the truncated PDF of $c/\langle c \rangle$ is

$$p(X = c/\langle c \rangle)|_{X > \xi} = \frac{1}{1 - \xi} \exp\left(-\frac{X - \xi}{1 - \xi}\right). \quad (5.2)$$

The slope (in a semilogarithmic graph) of the apparent PDF is therefore dependent on the chosen threshold, and the effect is significant if the threshold ξ is not $\ll 1$, which is the case here ($\xi = 0.5$, see Section 4.2). One implication is that, for meaningful comparisons, PDFs from different experiments, simulations, and times must be calculated over the same domain of $c/\langle c \rangle(t)$ (i.e. same value of ξ).

As discussed in section 4.2, this threshold is set to $\xi = 0.5$ at all times for all experiments and simulations. The cumulative distribution function associated with (5.2) is

$$P(c/\langle c \rangle < X)|_{c/\langle c \rangle > \xi} = 1 - \exp\left(-\frac{X - \xi}{1 - \xi}\right), \quad (5.3)$$

and the moments are

$$\langle X^k \rangle = (1 - \xi)^k \exp\left(\frac{\xi}{1 - \xi}\right) \Gamma\left(k + 1, \frac{\xi}{1 - \xi}\right), \quad (5.4)$$

where the incomplete gamma law is given by

$$\Gamma(k + 1, \xi) = \int_{\xi}^{\infty} x^k e^{-x} dx. \quad (5.5)$$

Comparison between the experimentally and numerically determined PDFs and the truncated exponential PDF given by (5.2) (grey line on figure 8) shows that the distribution of $c/\langle c \rangle$ is well described by the exponential distribution (5.2) for $c/\langle c \rangle$ smaller than 3 to 5, depending on t . According to equation (5.3), the probability of finding $c/\langle c \rangle < 3$ in the thermal is equal to 99.3%, which shows that the concentration in most of the thermal follows closely an exponential distribution, with the deviations at high concentrations being representative of less than 1% of the thermal cross-section surface area. Using the empirical cumulative density function calculated from the concentration maps rather than equation (5.3) gives similar results for experiments and simulations (see Appendix figures 20, 19, 21, 22).

Once the PDFs of concentration have converged toward a largely self-similar distribution with time, we compare the time-averaged PDF and examine the effects of Reynolds or Péclet numbers (figure 9). The PDFs of $c/\langle c \rangle$ are averaged in time (for $t/t_g > 10$) and averaged between runs for experiments (and between the two orthogonal plans for simulations). For

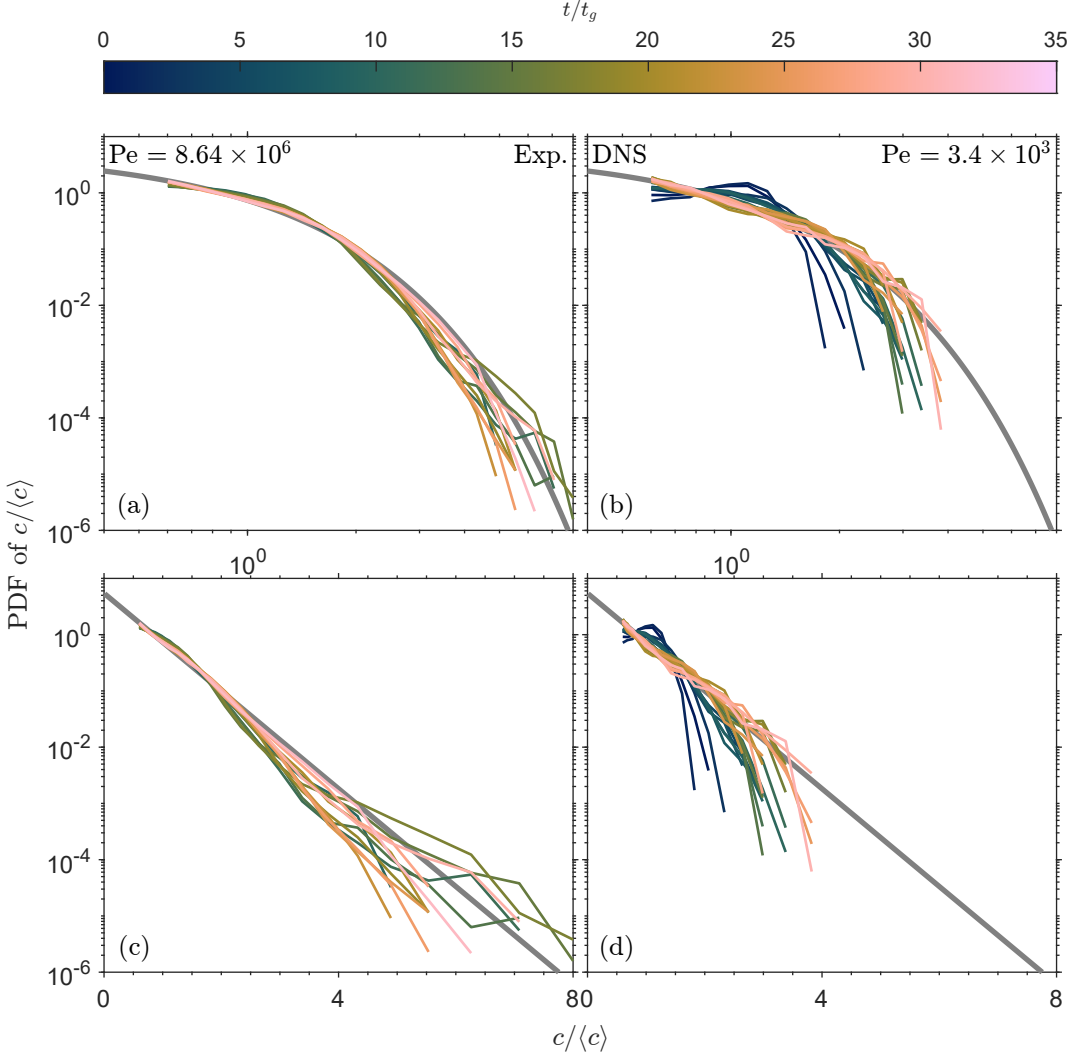


Figure 8: PDF of $c/\langle c \rangle$ as a function of $c/\langle c \rangle$ and time t/t_g for an experiment with $Re = 3452$ (a, c) ($Pe = 8.64 \times 10^6$) and a simulation at the same Re (b, d) ($Pe = 3.4 \times 10^3$). The top and bottom rows are log-log and semi-log plots, respectively. The gray lines show the exponential distribution defined by Eq. 5.2.

intermediate values of concentration, the PDF slope seems to be independent of Re or Pe (figure 9a). For high values of concentration ($c/\langle c \rangle > 5$), there are significant deviations from the exponential decrease, but without any clear trend with Reynolds or Péclet (figure 9b). These high values of concentration are related to the undiluted cores (see Section 4.2).

We can further evaluate our dimensional analysis and the exponential shape of the PDF using Eq. 2.16 and Eq. 5.4. From Eq. 5.4, we find that

$$\langle c^k \rangle = \langle X^k \rangle \langle c \rangle^k. \quad (5.6)$$

Dimensional analysis (Eq. 2.16) predicts that $\langle c \rangle \sim (t/t_g)^{-3/2} = (c_1 t/t_g)^{-3/2}$. The moments

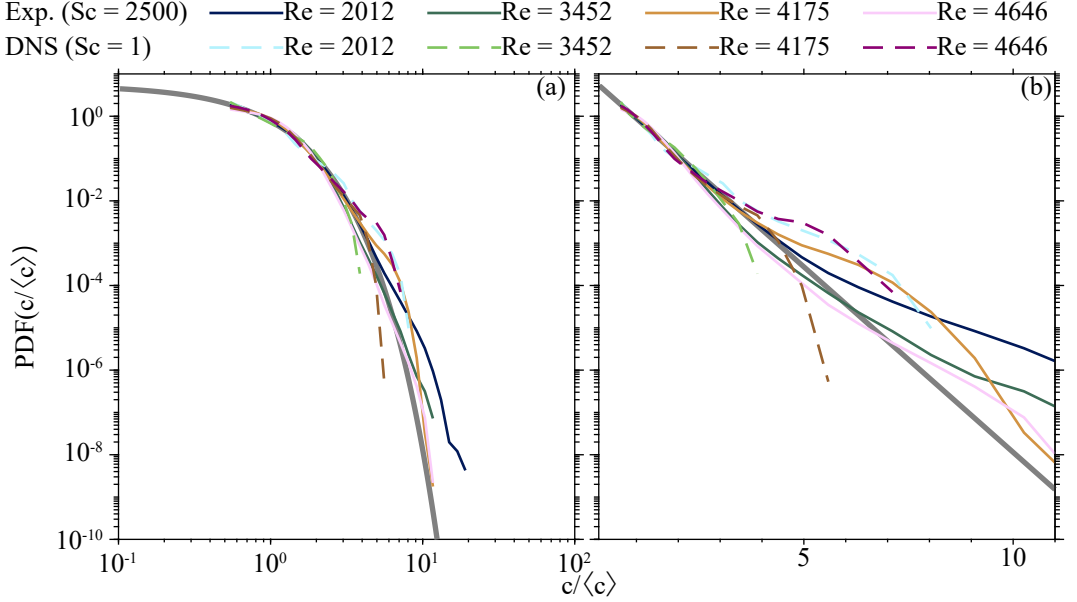


Figure 9: Temporal mean of the PDF of $c/\langle c \rangle$ as a function of $c/\langle c \rangle$ for all different Re numbers for the experiments (solid lines) and the simulations (dashed lines). (a) and (b) are log-log and semi-log plots, respectively. The gray line is the truncated exponential distribution (Eq. (5.2)).

of concentration are therefore predicted to evolve as

$$\langle c^k \rangle = (1 - \xi)^k \exp\left(\frac{\xi}{1 - \xi}\right) \Gamma\left(k + 1, \frac{\xi}{1 - \xi}\right) \left(c_1 \frac{t}{t_g}\right)^{-\frac{3}{2}k}. \quad (5.7)$$

In figure 6, the predicted moments are shown with grey dashed lines, using $c_1 = 2.0$, which is obtained by fitting experimental and numerical data with $\xi = 0.5$. The good agreement between the prediction of Eq. 5.7 (which assumes an exponential PDF) and the data gives further support to our proposition that the concentration PDF is exponential. It also shows that the time evolution of all the moments of c , and therefore of the PDF, can indeed be accurately predicted with a single fitting parameter (c_1).

Figure 10a shows the moment of concentration $\langle c/\langle c \rangle \rangle^k$ for different k as a function of time. All moments are shifted along the y-axis for better readability. The moments $\langle c/\langle c \rangle \rangle^k$ are almost constant with time in both experiments and simulations. Note that in figure 6, the evolution of the moment of concentration is well predicted by Eq. 5.7. Figure 10b shows the temporal mean of the moment of concentration $\overline{\langle c/\langle c \rangle \rangle^k}$ as a function of the predicted moment for a truncated exponential distribution (see Eq. 5.4). Moments of concentration are well explained by our truncated exponential distribution model, although the dispersion of the experimental and numerical values increases with k . Figure 10b shows no significant dependence on Reynolds or Schmidt numbers.

5.4. On the effect of Sc

The evolution of the concentration moments in a turbulent thermal seems independent of the Schmidt number Sc within the range $[1, 2500]$ presented here. In addition, the statistical distribution of c is also, at first order, independent of the diffusivity. However, differences do exist. First, we observe thicker structures or lamellae in the simulations than in the

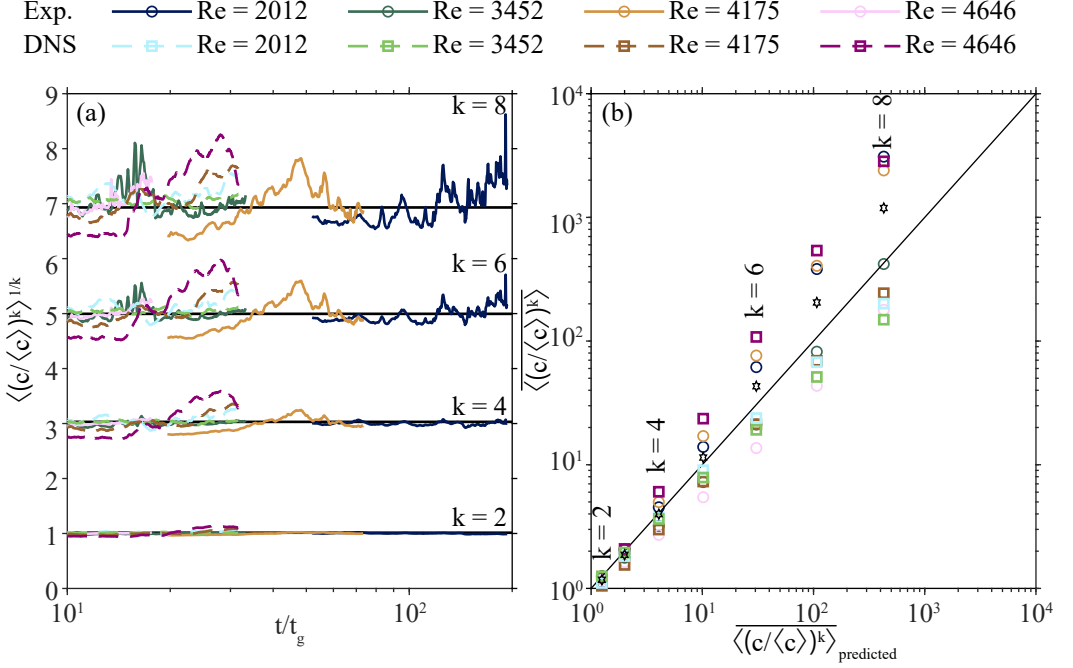


Figure 10: (a) Moment of concentration $\langle c/\langle c \rangle \rangle^k$, with $k = 2, 4, 6, 8$ as a function of time t/t_g for the mean of three experiments at each Re (solid lines) and the mean of two simulations at each Re (dashed lines). The black lines show the theoretical k th moment $E[X^k]$ according to Eq. 5.4. Note that the moments are shifted along the y-axis to help the visualization. (b) Temporal mean of the moment of concentration $\langle c/\langle c \rangle \rangle^k$ against the predicted moment $\langle c/\langle c \rangle \rangle^k_{\text{predicted}}$ (Eq. 5.4), with $k = 2$ to 8 . The black stars denote the mean of the k th moment for all Reynolds (experiments and simulations).

experiments (see figures 3 and 4). At any time, the diffusivity length scale is 50 times larger for the simulations than for the experiments.

Figure 9b reveals that the maximum concentration (compared to the mean concentration) is smaller in the $Sc = 1$ simulations compared to the $Sc = 2500$ experiments. This suggests that diffusion affects the evolution of the cores as maximum values of concentration correspond to the thermal cores (see figure 3c).

The exponential nature of the concentration PDF is unaffected by the diffusivity, as it is primarily determined by intermediate concentration values. Extrema values of concentration, which deviate from the exponential and are contained in the cores of turbulent thermal, might be better conserved in higher Péclet (lower diffusivity) turbulent thermal. A more thorough study of the evolution of the cores will be required to clarify the role of the mixing processes in the long-standing of the cores.

6. Discussion and conclusion

Early work on turbulent thermals - buoyant mass rising or sinking in a quiescent environment - primarily investigated their integral evolution, focusing on the concept of turbulent entrainment (Batchelor 1954; Morton *et al.* 1956; Turner 1986; Lecoanet & Jeevanjee 2019). More recently, experimental studies examined the internal structure of thermals by measuring their density and vorticity content (Bond & Johari 2005, 2010; Zhao *et al.* 2013). However, these studies have not examined the distributions of concentration in turbulent thermals, which is an insightful tool for investigating their internal structure and mixing dynamics.

In this study, we performed laboratory experiments and numerical simulations of turbulent thermals under similar conditions, and have analyzed the evolution of the moments and distribution of concentration. Our results show that the concentration fields of turbulent thermals are self-similar in time, except at high concentrations. Far from the source, the concentration distribution, normalized by the average concentration, is independent of time in both experiments and simulations (figure 8). The normalized moments of concentration are consistently constant over time (figure 10a). As discussed in section 1, this aligns with the fact that both Re and Pe remain constant over time when defined with the instantaneous radius and velocity (Eq. 2.2), resulting in constant normalized concentration moments in the asymptotic regime (Eq. 2.15). Self-similarity also requires that the typical length scales of concentration heterogeneities remain at a fixed ratio of the thermal size, and therefore evolve in proportion to r . The natural length scales of the problem – thermal size, diffusion length, Batchelor scale $\ell_B = (D/\gamma)^{1/2}$, where γ is the stretching rate of the concentration lamellae – appear to all have the same time dependence when far from the source, as shown below. The thermal radius increases as $t^{1/2}$ as predicted by equation 2.5. This is also the case for the diffusion length $(Dt)^{1/2}$. Concerning the Batchelor scale, dimensional analysis along the same lines as in Section 2.1 shows that, far from the source, the stretching rate should be of the form $\gamma = f_\gamma(Re)/t$, where $f_\gamma(Re)$ is an unknown function of Re . This predicts $\ell_B = f_\gamma(Re)^{-1/2}(Dt)^{1/2}$.

The stationary nature of the distribution of $c/\langle c \rangle$, i.e. the self-similar behavior, can be qualitatively understood as resulting from a balance between the competing effects of homogenization within the thermal and continuous addition of ambient liquid through engulfment. This is well illustrated by the fact that the ratio of the standard deviation to the mean of concentration $\sqrt{\sigma^2}/\langle c \rangle$ is constant with time (equal to 1 for an exponential distribution), which contrasts with the evolution of stirred concentration fields in confined spaces, for which the ratio $\sqrt{\sigma^2}/\langle c \rangle$ tends towards 0 as mixing proceeds. However, the details of the mechanisms by which the stationary distribution is maintained have yet to be understood and modeled.

Our interpretation of self-similarity contrasts with the findings of Zhao *et al.* (2013), who found that the overall thermal does not show a self-similar evolution, although the cores do evolve self-similarly. This conclusion relies on a different measure of self-similarity, where the stability of ensemble-averaged radial vorticity and density profiles is assessed over the development of the thermal. The profiles are normalized by their maximum value, located in the cores, which differs from our results, where we normalize the concentration distribution by the average concentration of the thermal. Since the maximum concentration decreases more slowly than the average concentration, this may explain why self-similarity is observed in the cores but not in the overall thermal. Normalizing the profiles by quantities averaged over the thermal could result in a self-similar evolution of the profiles, except in the core, which is consistent with our findings.

Our results reveal that the distribution of concentration is well approximated by a parameter-free exponential PDF (figure 9 and 10b), except at large concentrations where

the distribution is relatively scattered. The departure from exponential behavior seems to be related to the high concentration cores of the thermal, and suggests a locally different mixing dynamics. The cores of the thermal are protected from mixing, whereas the peripheral region is mixed more efficiently (figure 2). This is consistent with the process of turbulent entrainment, which engulfs the surrounding fluid in the peripheral region toward the center of the thermal. The cores around which the thermal wraps remain relatively undiluted. This qualitative observation is supported by the concentration PDF, as the cores of the thermal correspond to the highest concentration values (figure 3 and 4). The slower decrease in maximum concentration compared to the average confirms that the cores are relatively protected from mixing (figure 5b). Furthermore, the maximum concentration decreases slower in the experiments than in the simulations (figure 5c), possibly indicating a diffusive mixing process since experiments have a lower diffusivity.

The distribution of concentration characterizes the fluid mixtures described as a superposition of concentration lamellae (Villermaux 2019). In expanding systems, such as turbulent jets (Duplat et al. 2010), exponential tails result from the distribution of elongation events and mixing times among non-interacting lamellae. In confined systems, such as turbulent plumes (Villermaux & Duplat 2003; Duplat & Villermaux 2008) and porous media flow (Le Borgne et al. 2015), they arise from kinetic aggregation of lamellae, leading to the self-convolution of concentration distributions. In between these extreme situations, flows involving partial aggregation also produce exponential tails (Le Borgne et al. 2013, 2017). In the aggregation mechanism, the concentration PDF is related to the number of aggregations (number of lamellae in a given radius, see Duplat & Villermaux (2008); Le Borgne et al. (2017)), which increases with time as the mixing occurs. Since the PDF of concentration normalized by the mean is independent of time, our distribution may represent an effective aggregation number in the asymptotic regime. A dynamic equilibrium can be formed between a homogeneous fluid (high aggregation inside the thermals, where correlated aggregation might occur (Heyman et al. 2024)) and a fresh fluid (without aggregation) on a characteristic entrainment time scale. This specific configuration would lead to an apparent aggregation number close to 1 in the concentration distributions.

An unexpected observation is the very weak effect of diffusion on the PDFs of concentration, as shown by the comparison of experiments and numerical simulations carried out at the same values of the Reynolds number, but differing by a factor of 2500 in terms of Peclet numbers. In both cases, the concentration distribution is well described by an exponential PDF. Across the range of Reynolds and Péclet numbers examined in our experiments and simulations, the concentration distributions are mostly independent of Re and Pe (figures 9 and 10), showing a weak effect of viscosity and diffusion on the distributions. At the same Re , the concentration maximum is higher in experiments ($Sc = 2500$) than in numerical simulations ($Sc = 1$), suggesting a marginal dependency on Pe , possibly through diffusive homogenization of the cores. However, diffusivity strongly affects the spatial structure of the concentration field, as shown by notably finer structures in the experiments than in simulations (figure 2c-d). This could be further analyzed with the distribution of the concentration increments and their moments, known as structure functions (Le Borgne et al. 2017; Villermaux 2019). This approach would help characterize the mixing process that underlies the exponential distribution.

Supplementary data.

Here is a link to a video of the 4 experiments at each Reynolds. [video](#)

Acknowledgements. LH thanks Daniel Lecoanet for helping implement Dedalus into the HPC of Université Grenoble Alpes and for the data provided for the large-resolution simulations. All the 3D simulations

presented in this paper were performed using the GRICAD infrastructure (<https://gricad.univ-grenoble-alpes.fr>), supported by Grenoble research communities.

Funding. This work was supported by the European Research Council (ERC) under the European Unions Horizon 2020 research and innovation programme (grant number 716429). ISTerre is part of Labex OSUG@2020 (ANR10 LABX56).

Declaration of interests. The authors report no conflict of interest.

Data availability statement.

Author ORCIDs. L. Huguet, <https://orcid.org/0000-0002-5532-6302>; V. Lherm, <https://orcid.org/0000-0001-5814-0637>; R. Deguen, <https://orcid.org/0000-0002-6883-0655>; T. Le Borgne, <https://orcid.org/0000-0001-9266-9139>; J. Heyman, <https://orcid.org/0000-0002-0327-7924>

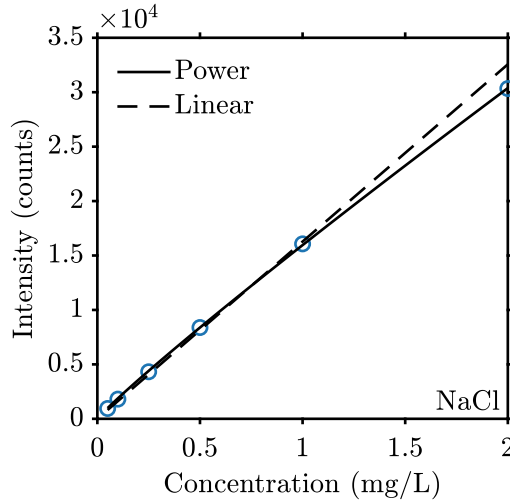


Figure 11: Fluorescence light intensity as a function of Rhodamine 6G concentration in aqueous solutions of NaCl. The solid line corresponds to a power law of the form $I = ac^b$ fitted to the experimental data, with $a = (1.60 \pm 0.01) \times 10^4$ and $b = 0.93 \pm 0.01$. The dashed line corresponds to a power law of the form $I = ac$ fitted to the experimental data for $c \leq 1$ mg/L, with $a = (1.63 \pm 0.02) \times 10^4$.

Appendix A. Intensity-Concentration Calibrations

The determination of the concentration field uses a relationship between the fluorescence intensity of Rhodamine 6G and its concentration. This relationship is independently calibrated for each experimental case (A, B, C, and D), as the initial concentrations vary from one case to another, and the fluorescence intensity slightly depends on the NaCl concentration. For each case, the fluorescence intensity of the solution contained in the tube is measured under conditions identical to the experiments to account for potential absorption effects along the path of the laser sheet. The initial aqueous solution is gradually diluted with water to consider the concurrent variation in salt concentration along with the variation in fluorescent dye concentration. Figure 11 shows one of the calibrations of the light intensity I as a function of the concentration c of Rhodamine 6G. When $c \rightarrow 0$, the light intensity should increase linearly with the dye concentration and attenuate at high concentrations. This is indeed the case when $c \gtrsim 1$ mg/L. This attenuation could also be related to interactions with NaCl, leading to the formation of aggregates that reduce the fluorescence intensity. To account for this effect at high concentration, the intensity-concentration calibration thus employs a power law of the form $I = ac^b$ rather than a linear law.

Appendix B. Supplementary figures at different Reynolds numbers

Figure 12 shows the evolution of the thermal for experiments and simulations for all Reynolds numbers. Standard deviation of the concentration field for the entire time series and each of the three experiments or two orthogonal plans of 3D simulations. Red dashed lines correspond to the evolution of the radius of the thermal with depth $r = \alpha z$, using $\alpha = 0.18$.

The appendix B also contains figures of the PDF of concentration for the different experiments and simulations presented in this manuscript. Figures 13 and 14, and 15 show the PDF of concentration for 3 Reynolds numbers. Figures 16, 17, and 18 are the PDFs of the concentration normalized by the mean of c . Figure 19, 20, 21, and 22 are the cumulative PDFs of the $c/\langle c \rangle$ (see 8). Figure 23 shows the PDFs of the concentration normalized by

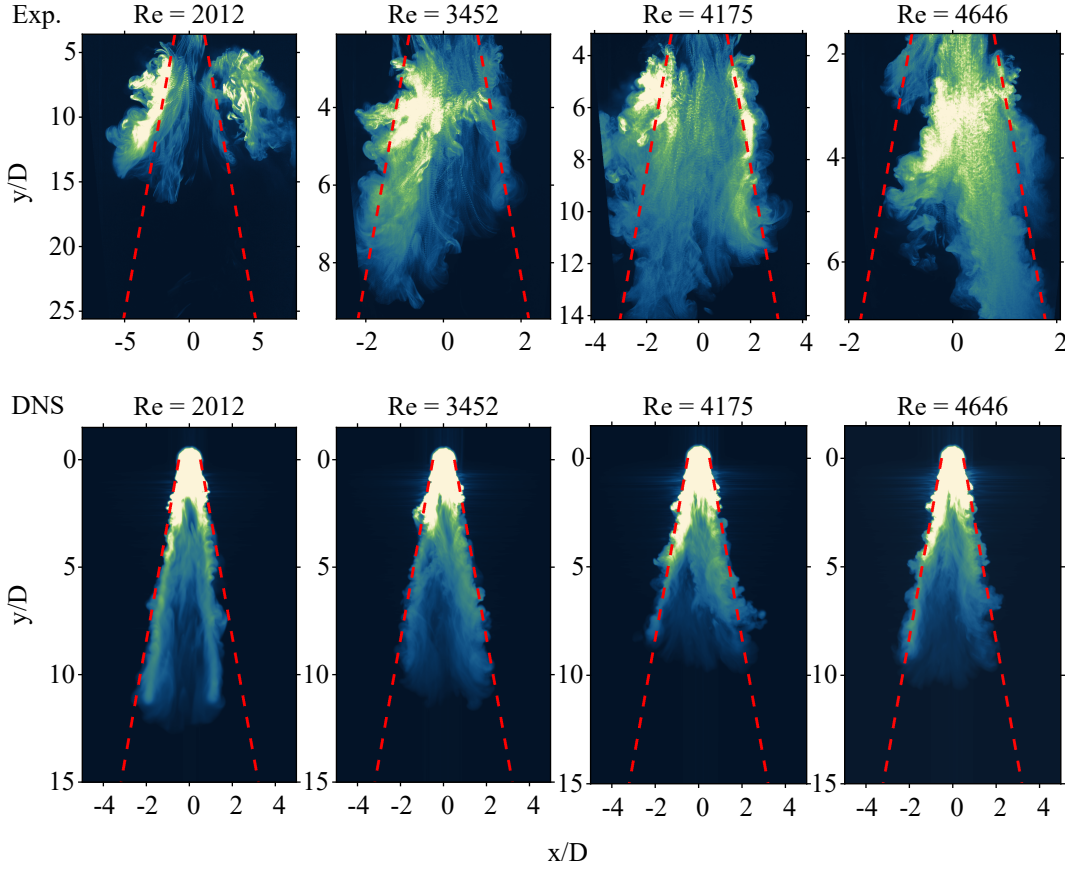


Figure 12: Standard deviation of the concentration field for the entire time series and each of the three experiments or two orthogonal plans of 3D simulations. Red dashed lines correspond to the evolution of the radius of the thermal with depth $r = \alpha z$, using $\alpha = 0.18$.

the mean of c for two simulations with the same Reynolds but with two different resolutions $256 \times 256 \times 512$ and $512 \times 512 \times 1024$.

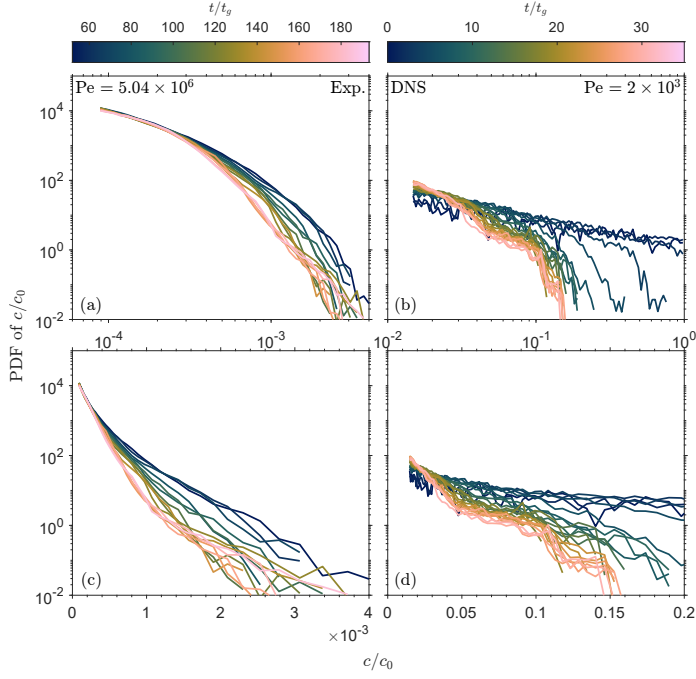


Figure 13: PDF of c as a function of c and time t/t_g with a given $Re = 1012$ for one of the three experiments (a,c) ($Pe = 5.04 \times 10^6$) and a simulation (b,d) ($Pe = 2.8 \times 10^3$). The top and bottom rows are log-log and semi-log plots, respectively.

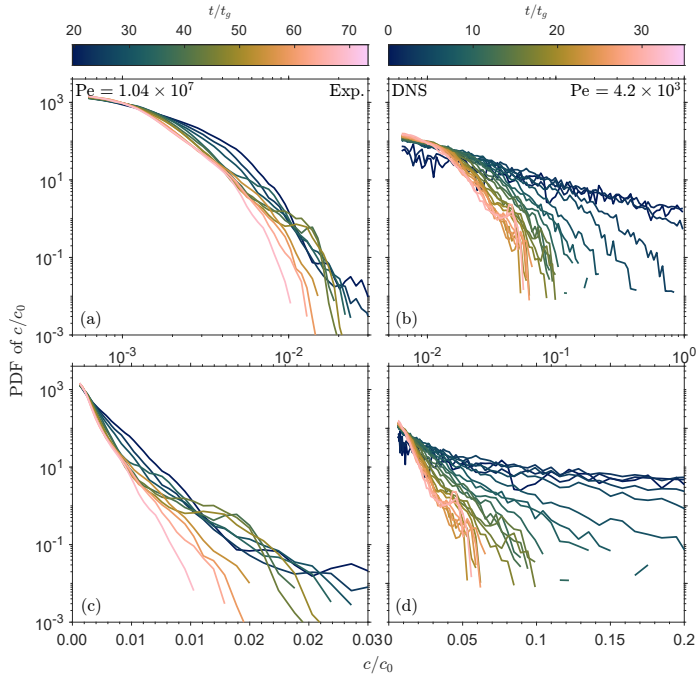


Figure 14: Same as figure 13 for $Re = 4175$ ($Pe = 1.04 \times 10^7$ for experiments and $Pe = 4.2 \times 10^3$ for simulation).

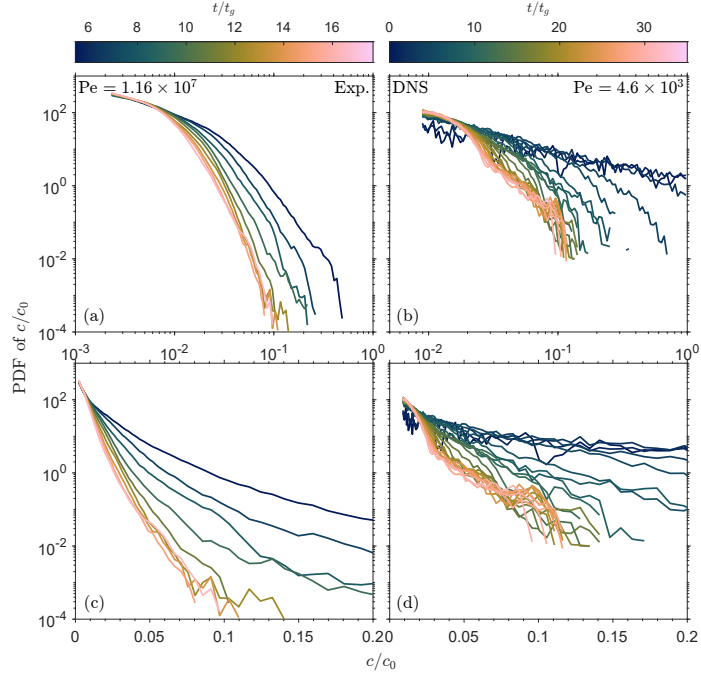


Figure 15: Same as figure 13 for $Re = 4646$ ($Pe = 1.16 \times 10^7$ for experiments and $Pe = 4.6 \times 10^3$ for simulation).

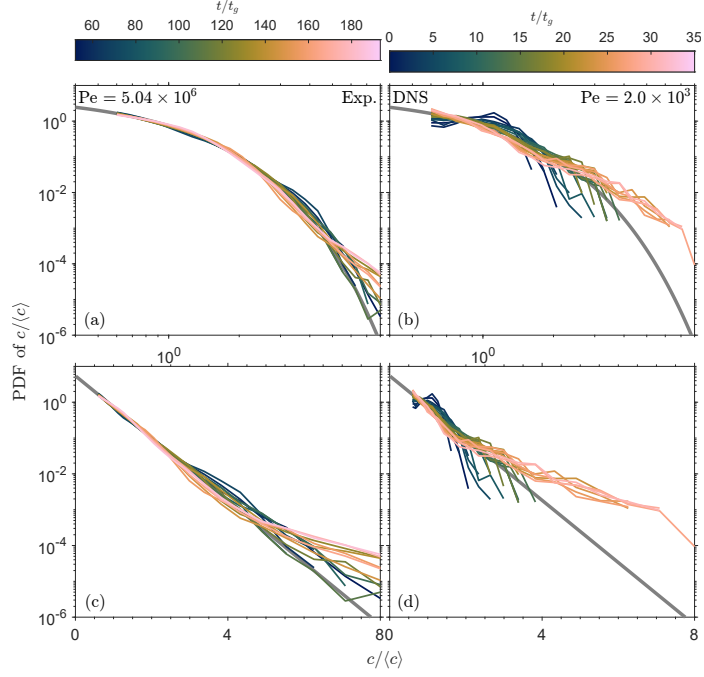


Figure 16: PDF of $c/\langle c \rangle$ as a function of $c/\langle c \rangle$ and time t/t_g with a given $Re = 2012$ for an experiment (a, c) ($Pe = 5.04 \times 10^6$) and a simulation (b, d) ($Pe = 2.0 \times 10^3$). The top and bottom rows are log-log and semi-log plots, respectively. The gray denotes the equation of the exponential distribution 5.2.

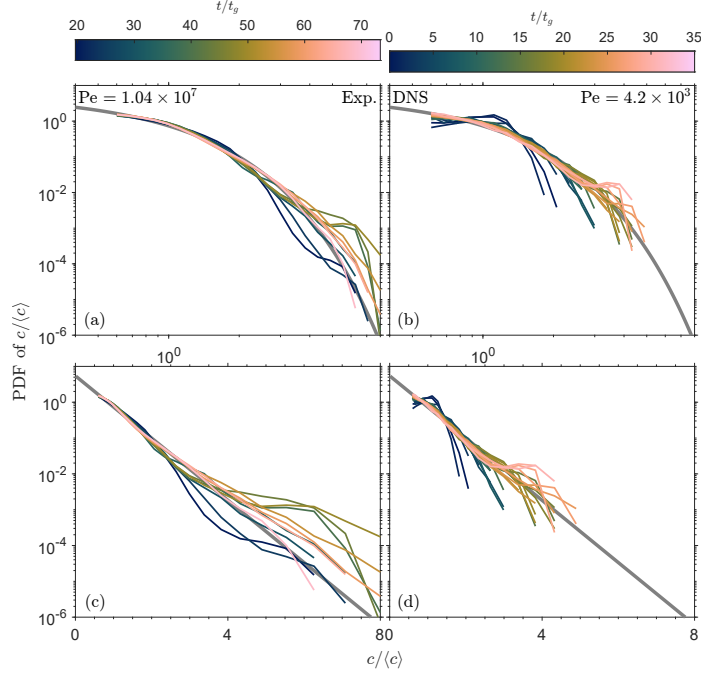


Figure 17: Same as figure 16 for $Re = 4175$ ($Pe = 1.04 \times 10^7$ for experiments and $Pe = 4.2 \times 10^3$ for simulation).

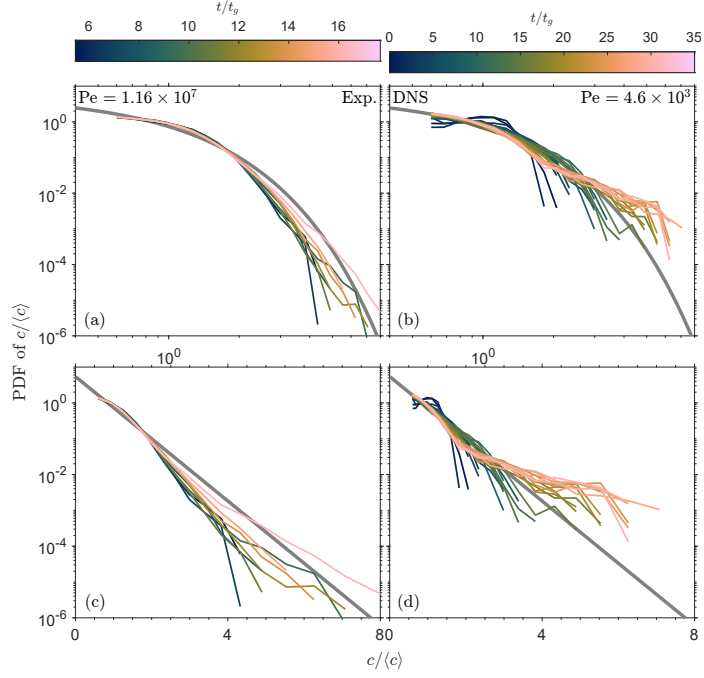


Figure 18: Same as figure 16 for $Re = 4646$ ($Pe = 1.16 \times 10^7$ for experiments and $Pe = 4.6 \times 10^3$ for simulation).

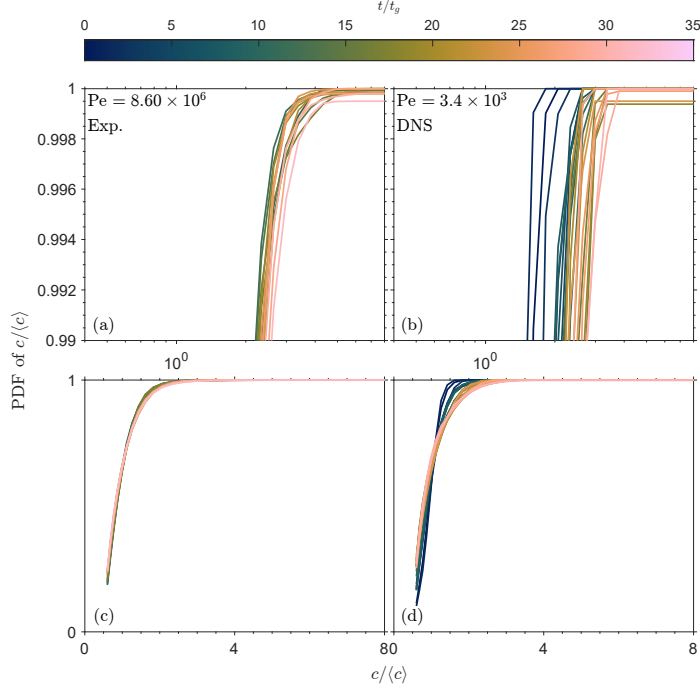


Figure 19: Cumulative PDF of $c/\langle c \rangle$ as a function of $c/\langle c \rangle$ and time t/t_g for an experiment with $Re = 3452$ (a, c) ($Pe = 8.64 \times 10^6$) and a simulation at the same Re (b, d) ($Pe = 3.4 \times 10^3$). The top and bottom rows are log-log and linear-linear plots, respectively.

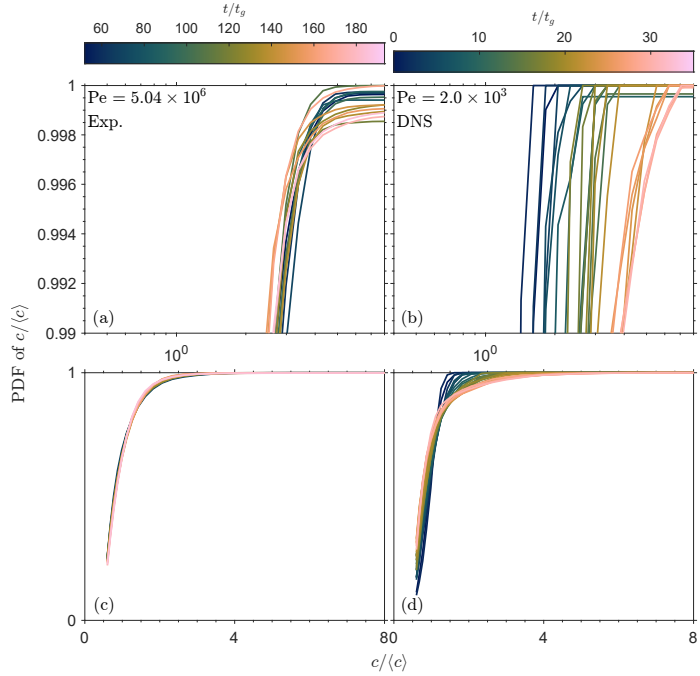


Figure 20: Same as figure 19 for $Re = 2012$ ($Pe = 5.04 \times 10^6$ for experiments and $Pe = 2.0 \times 10^3$ for simulation).

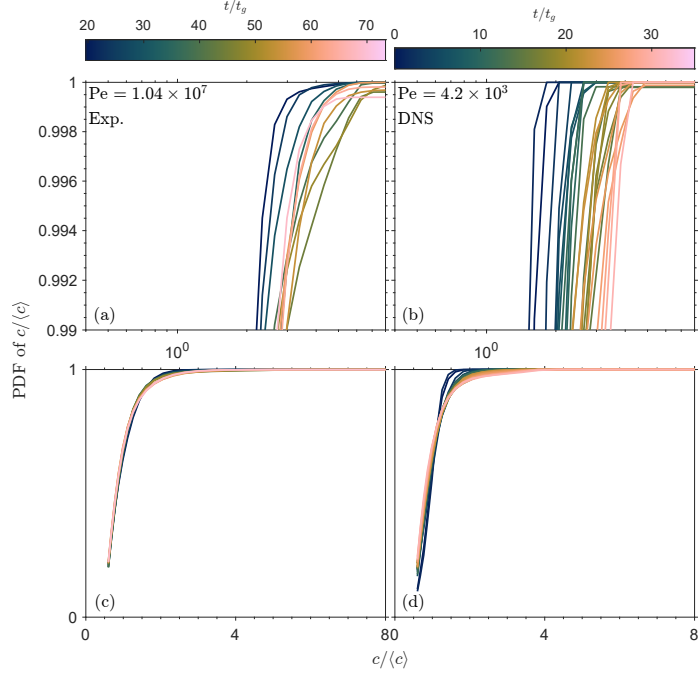


Figure 21: Same as figure 19 for $Re = 4175$ ($Pe = 1.04 \times 10^7$ for experiments and $Pe = 4.2 \times 10^3$ for simulation).

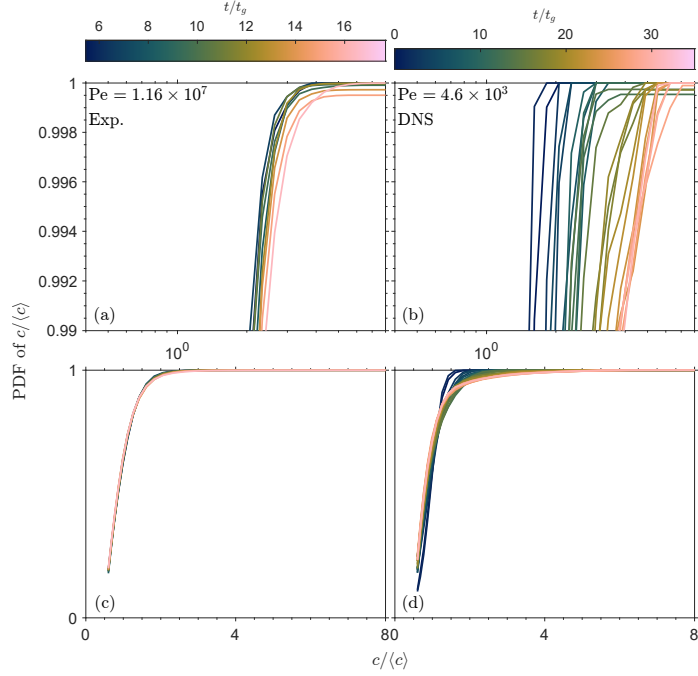


Figure 22: Same as figure 16 for $Re = 4646$ ($Pe = 1.16 \times 10^7$ for experiments and $Pe = 4.6 \times 10^3$ for simulation).

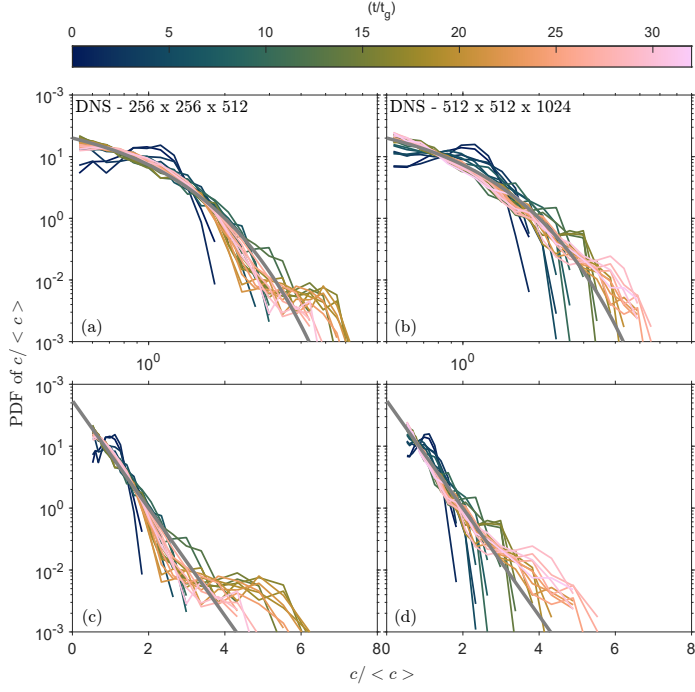


Figure 23: PDF of $c/\langle c \rangle$ as a function of $c/\langle c \rangle$ and time t/t_g with a given $Re = 4631$ for a simulation with a resolution of $256 \times 256 \times 512$ (a, c) and with a resolution of $512 \times 512 \times 1024$ (b, d). The top and bottom rows are log-log and semi-log plots, respectively. The gray denotes the equation of the exponential distribution 5.2.

REFERENCES

- BAT, RG, BIGONI, RA & ROWLAND, DJ 1984 Temperature-field structure within atmospheric buoyant thermals. *Journal of Fluid Mechanics* **141**, 1–25.
- BATCHELOR, G. K. 1954 Heat convection and buoyancy effects in fluids. *Quarterly Journal of the Royal Meteorological Society* **80** (345), 339–358.
- BLYTH, ALAN M, COOPER, WILLIAM A & JENSEN, JØRGEN B 1988 A study of the source of entrained air in montana cumuli. *Journal of Atmospheric Sciences* **45** (24), 3944–3964.
- BLYTH, ALAN M, LASHER-TRAPP, SONIA G & COOPER, WILLIAM A 2005 A study of thermals in cumulus clouds. *Quarterly Journal of the Royal Meteorological Society: A journal of the atmospheric sciences, applied meteorology and physical oceanography* **131** (607), 1171–1190.
- BOND, D & JOHARI, H 2005 Effects of initial geometry on the development of thermals. *Experiments in fluids* **39**, 591–601.
- BOND, D & JOHARI, H 2010 Impact of buoyancy on vortex ring development in the near field. *Experiments in fluids* **48**, 737–745.
- BURNS, KEATON J, VASIL, GEOFFREY M, OISHI, JEFFREY S, LECOANET, DANIEL & BROWN, BENJAMIN 2016 Dedalus: Flexible framework for spectrally solving differential equations. *Astrophysics Source Code Library* pp. ascl–1603.
- BURNS, KEATON J, VASIL, GEOFFREY M, OISHI, JEFFREY S, LECOANET, DANIEL & BROWN, BENJAMIN P 2020 Dedalus: A flexible framework for numerical simulations with spectral methods. *Physical Review Research* **2** (2), 023068.
- BUSH, JOHN WM, THURBER, BA & BLANCHETTE, F 2003 Particle clouds in homogeneous and stratified environments. *Journal of Fluid Mechanics* **489**, 29–54.
- DUPLAT, J., INNOCENTI, C. & VILLERMAUX, E. 2010 A nonsequential turbulent mixing process. *Physics of Fluids* **22** (3), 035104.
- DUPLAT, J. & VILLERMAUX, E. 2008 Mixing by random stirring in confined mixtures. *Journal of Fluid Mechanics* **617**, 51–86.
- GENDRON, P-O, AVALTRONI, F & WILKINSON, KJ 2008 Diffusion coefficients of several rhodamine derivatives as determined by pulsed field gradient–nuclear magnetic resonance and fluorescence correlation spectroscopy. *Journal of fluorescence* **18** (6), 1093–1101.
- GHAEM-MAGHAMI, E. & JOHARI, H. 2006 Concentration field measurements within isolated turbulent puffs. *Journal of Fluids Engineering* **129** (2), 194–199.
- HAYNES, WILLIAM M 2014 CRC handbook of chemistry and physics. CRC press.
- HEYMAN, J., VILLERMAUX, E., DAVY, P. & LE BORGNE, T. 2024 Mixing as a correlated aggregation process. *Journal of Fluid Mechanics* **992**, A6.
- JOHARI, HAMID 1992 Mixing in thermals with and without buoyancy reversal. *Journal of the atmospheric sciences* **49** (16), 1412–1426.
- LAI, ADRIAN CH, ZHAO, BING, LAW, ADRIAN WING-KEUNG & ADAMS, E ERIC 2015 A numerical and analytical study of the effect of aspect ratio on the behavior of a round thermal. *Environmental Fluid Mechanics* **15**, 85–108.
- LANDEAU, MAYLIS, DEGUEN, RENAUD & OLSON, PETER 2014 Experiments on the fragmentation of a buoyant liquid volume in another liquid. *Journal of fluid mechanics* **749**, 478–518.
- LE BORGNE, TANGUY, DENTZ, MARCO & VILLERMAUX, EMMANUEL 2013 Stretching, Coalescence, and Mixing in Porous Media. *Physical Review Letters* **110** (20), 204501.
- LE BORGNE, T., DENTZ, M. & VILLERMAUX, E. 2015 The lamellar description of mixing in porous media. *Journal of Fluid Mechanics* **770**, 458–498.
- LE BORGNE, T., HUCK, P. D., DENTZ, M. & VILLERMAUX, E. 2017 Scalar gradients in stirred mixtures and the deconstruction of random fields. *Journal of Fluid Mechanics* **812**, 578–610.
- LECOANET, DANIEL & JEEVANJEE, NADIR 2019 Entrainment in resolved, dry thermals. *Journal of the Atmospheric Sciences* **76** (12), 3785–3801.
- MARCUS, DANIEL L & BELL, JOHN B 1992 The structure and evolution of the vorticity and temperature fields in thermals. *Theoretical and Computational Fluid Dynamics* **3** (6), 327–344.
- MCKIM, BRETT, JEEVANJEE, NADIR & LECOANET, DANIEL 2020 Buoyancy-driven entrainment in dry thermals. *Quarterly Journal of the Royal Meteorological Society* **146** (726), 415–425.
- MIDDLETON, JASON H & MUMFORD, PETER J 2023 Thermals from finite sources in stable and unstable environments. *Journal of Fluid Mechanics* **960**, A41.

- MORRISON, HUGH 2025 Entrainment, detrainment, and dilution of dry and moist atmospheric thermals. *Journal of the Atmospheric Sciences* **82** (2), 361–389.
- MORRISON, HUGH, JEEVANJEE, NADIR, LECOANET, DANIEL & PETERS, JOHN M 2023 What controls the entrainment rate of dry buoyant thermals with varying initial aspect ratio? *Journal of the Atmospheric Sciences* **80** (11), 2711–2728.
- MORRISON, HUGH, JEEVANJEE, NADIR & YANO, JUN-ICHI 2022 Dynamic pressure drag on rising buoyant thermals in a neutrally stable environment. *Journal of the Atmospheric Sciences* **79** (11), 3045–3063.
- MORTON, BR, NGUYEN, KC & CRESSWELL, RW 1994 Similarity and self-similarity in the motion of thermals and puffs. *Recent research advances in the fluid mechanics of turbulent jets and plumes* pp. 89–116.
- MORTON, BR, TAYLOR, GEOFFREY & TURNER, JS 1956 Turbulent gravitational convection from maintained and instantaneous sources. In *Proceedings of the Royal Society of London A: Mathematical, Physical and Engineering Sciences*, , vol. 234, pp. 1–23. The Royal Society.
- ORLANDI, P & CARNEVALE, GF 2020 Numerical simulations of thermals with and without stratification. *Journal of Fluid Mechanics* **899**, A37.
- ROMPS, DAVID M & CHARN, ALEXANDER B 2015 Sticky thermals: Evidence for a dominant balance between buoyancy and drag in cloud updrafts. *Journal of the Atmospheric Sciences* **72** (8), 2890–2901.
- ROMPS, DAVID M & KUANG, ZHIMING 2010 Do undiluted convective plumes exist in the upper tropical troposphere? *Journal of the Atmospheric Sciences* **67** (2), 468–484.
- SCORER, ROBERT S 1957 Experiments on convection of isolated masses of buoyant fluid. *Journal of Fluid Mechanics* **2** (6), 583–594.
- TAYLOR, GI 1946 *Dynamics of a mass of hot gas rising in air*, , vol. 919. Technical Information Division, Oak Ridge Operations.
- TERADA, A. & IDA, Y. 2007 Kinematic features of isolated volcanic clouds revealed by video records. *Geophys. Res. Lett.* **34**, L01305.
- TURNER, JOHN STEWART 1979 *Buoyancy effects in fluids*. Cambridge Univ. Press.
- TURNER, J. S. 1986 Turbulent entrainment: The development of the entrainment assumption, and its application to geophysical flows. *Journal of Fluid Mechanics* **173**, 431–471.
- VILLERMAUX, EMMANUEL 2019 Mixing Versus Stirring. *Annual Review of Fluid Mechanics* **51** (1), 245–273.
- VILLERMAUX, E. & DUPLAT, J. 2003 Mixing as an Aggregation Process. *Physical Review Letters* **91** (18), 184501.
- VYBHAV, GR & RAVICHANDRAN, SANDHANAKRISHNAN 2022 Entrainment in dry and moist thermals. *Physical Review Fluids* **7** (5), 050501.
- WOODWARD, B. 1958 A theory of thermal soaring. *Swiss Aero. Revue, OSTIV Section*, **6**, 131.
- WOODWARD, B. 1959 The motion in and around isolated thermals. *Quarterly Journal of the Royal Meteorological Society* **85** (364), 144–151.
- YANO, J-I 2014 Basic convective element: Bubble or plume? a historical review. *Atmospheric Chemistry and Physics* **14** (13), 7019–7030.
- YEE, EUGENE, CHAN, R, KOSTENIUK, PR, CHANDLER, GM, BILTOFT, CA & BOWERS, JF 1994 Concentration fluctuation measurements in clouds released from a quasi-instantaneous point source in the atmospheric surface layer. *Boundary-layer meteorology* **71** (4), 341–373.
- YEE, EUGENE, CHAN, R, KOSTENIUK, PR, CHANDLER, GM, BILTOFT, CA & BOWERS, JF 1995 The vertical structure of concentration fluctuation statistics in plumes dispersing in the atmospheric surface layer. *Boundary-Layer Meteorology* **76** (1), 41–67.
- ZHAO, B, LAW, AWK, LAI, ACH & ADAMS, EE 2013 On the internal vorticity and density structures of miscible thermals. *Journal of Fluid Mechanics* **722**, R5.